AMINE-IMPREGNATED BLOCK COPOLYMER DIRECTED ASYMMETRIC POROUS TITANIA ADSORBENTS FOR CARBON-DIOXIDE CAPTURE

A Thesis

Presented to the Faculty of the Graduate School

of Cornell University

In Partial Fulfillment of the Requirements for the Degree of

Master of Science

by

Ningning Yang

August 2025

ABSTRACT

Amine-functionalized porous solid sorbents are widely regarded as leading candidates for post-combustion CO_2 capture. While mesoporous MCM-41 is a benchmark material due to its tunable mesopores, its poor hydrothermal stability limits industrial applications. Here, asymmetric TiO_2 films fabricated via block copolymer self-assembly and non-solvent induced phase separation (SNIPS) offer a robust, tunable alternative. Compared to alternating gyroidal TiO_2 controls, they exhibit improved processability and reduced amine usage while achieving equivalent loading. CO_2 adsorption studies across varying temperatures, flow rates, concentrations, and poly(ethylenimine) (PEI) loadings reveal that the asymmetric sorbents consistently outperformed their gyroidal counterparts, achieving 2.5–3 times higher uptake. A composite kinetic model identified a three-stage mechanism, with the time scales and relative contributions of each stage strongly dependent on adsorbent morphology. These findings highlight how structural asymmetry—through a balance of enhanced mass transport and amine-accessible surface area—improves adsorption efficiency and overall adsorbent performance.

BIOGRAPHICAL SKETCH

Ningning Yang was born in Ningbo, China, where she spent her early years and completed her primary and secondary education. Fascinated by hands-on laboratory experiments since high school, she chose to major in Macromolecular Materials and Engineering at Fudan University in Shanghai. During her undergraduate years, she spent considerable time on designing posters for student organizations and clubs using Photoshop – an unexpected experience that later proved helpful in making scientific schematics.

Ningning found her passion for research during her undergraduate research under the guidance of Prof. Zhihong Nie, where she successfully synthesized amphiphilic inorganic/polymer Janus particles for coating applications. In the fall of 2023, she joined the Wiesner Group at Cornell University as a Master's student in Materials Science and Engineering. Her research focused on the fabrication and functionalization of asymmetric TiO_2 films for carbon capture, combining block copolymer self-assembly with sol-gel chemistry and non-solvent induced phase separation (NIPS). After graduating from Cornell, Ningning will continue her exploration of sustainable polymers at KTH Royal Institute of Technology in Sweden.

Dedicated to my Family and Friends

ACKNOWLEDGMENTS

I would like to sincerely thank my advisor, Prof. Uli Wiesner, for his patient guidance, scientific rigor, and invaluable support throughout this project. I have learned a lot from his mentorship, both in research and in thinking critically. I would like to thank Prof. Yu Zhong for his continued support, and Prof. Mike Thompson for his timely help at the final stage of my thesis.

I'm deeply grateful to my mentor Dr. Lilly Tsaur, who helped me adapt to studying abroad and generously shared her knowledge and skills. I also appreciate the help and encouragement from my group members, including Dr. Fei Yu, Dr. Will Tait, Dr. Joe Chang, William Moore, Danni Tang, and the entire lab, over the past two years.

Thanks also to my collaborators in the Milner Group in the Chemistry Department, Prof. Phillip Milner and graduate student Alexandra Lim, for their helpful suggestions and experimental support.

Finally, I would like to thank my family for their unwavering belief in me and my friends for keeping me grounded. None of this would have been possible without them.

TABLE OF CONTENTS

LIST OF FIGURES

LIST OF TABLES

LIST OF ABBREVIATIONS

BCP – Block copolymer

SA – Self-assembly

ISO – Poly(isoprene-*block*-styrene-*block*-ethylene oxide)

NIPS – Non-solvent induced phase separation

SNIPS – Self-assembly and non-solvent induced phase separation

TiO_2 – Titania

ISV – Poly(isoprene-*block*-styrene-*block*-4-vinylpyridine)

PEI – Poly(ethylenimine)

EISA – Evaporation-induced self-assembly

TGA – Thermogravimetric analysis

THF – Tetrahydrofuran

DOX – 1,4-Dioxane

DI – Deionized

MeOH – Methanol

GPC – Gel permeation chromatograph

NMR – Nuclear magnetic resonance

SEM – Scanning electron microscopy

SAXS – Small-angle X-ray scattering

WAXS – Wide-angle X-ray scattering

G^A – Alternating gyroid

BET – Brunauer-Emmett-Teller

BJH – Barrett-Joyner-Halenda

TEPA – Tetraethylenepentamine

CHAPTER 1

INTRODUCTION

Carbon dioxide (CO_2) is a major greenhouse gas contributing to global warming and climate change[1]. The main CO_2 emissions are from burning of fossil fuels such as coal, natural gas and oil, to generate electricity, provide industrial and residential heating as well as power transportation tools[2]. A number of strategies have been developed for CO_2 mitigation, including utilization of renewable energy and nuclear power, improvement of production efficiency in power systems, and development of clean technologies[3]. However, these approaches are considered very costly to scaling up and lacking public support. As a result, fossil fuels are expected to remain a major portion of global energy in the near future[4]. Moreover, activities like aviation and iron smelting, are impossible to run without releasing CO_2.

In response to these challenges, massive efforts have been devoted to preventing the release of CO_2 emissions into the atmosphere. Carbon capture, utilization, and storage (CCUS) has emerged as a promising and cost-effective pathway for large-scale emission reduction. Since CO_2 capture is the initial and most crucial step in CCUS, the development of capture technologies and materials is essential for enabling broad industrial use.

An ideal CO_2 adsorbent must meet several performance criteria: high adsorption capacity and selectivity for CO_2, strong chemical and thermal stability, fast kinetics of adsorption and desorption, compatibility with regeneration protocols, and cost-

effectiveness for scale-up[5]. Aqueous amine solutions, which have long been employed for CO_2 capture and are widely accepted in industrial applications, exhibit high selectivity and capacity for CO_2 but suffer from several significant limitations. Low amine concentrations are required to mitigate corrosion, which lowers overall capture capacity[6]. Additionally, high regeneration temperatures are needed due to the high heat capacity of water and strong CO_2–amine binding enthalpy, leading to significant parasitic energy losses, which make up about 25–30% of the net power output of a plant[7]. Additional limitations include the solvent volatility, potential for amine leakage, and degradation of the amine under thermal or oxidative conditions.

As an alternative, a wide range of porous solid materials such as zeolites, silica, and metal-organic frameworks (MOFs) have been explored for CO_2 capture[8]. These materials offer advantages including low heat capacity and high surface areas, which enable more energy-efficient adsorption-desorption cycling. However, many of these solid adsorbents suffer from poor CO_2 selectivity in humid environments due to competitive adsorption of water vapor, which significantly diminishes their CO_2 uptake[9]. This limitation has hindered their practical deployment in real-world gas streams, where moisture is typically present.

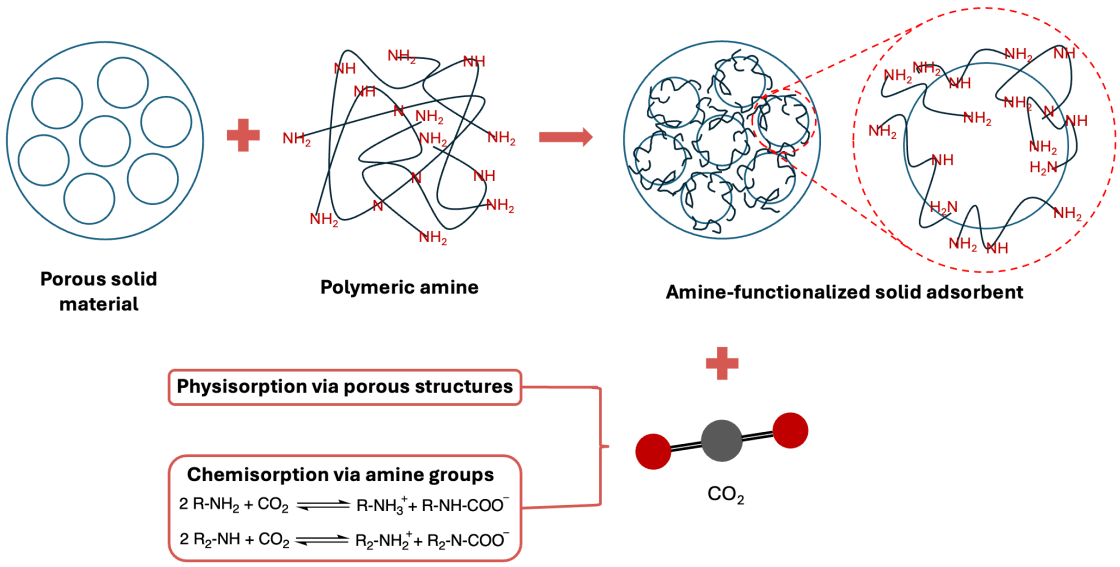

Figure 1.1. Schematic of functionalization of porous solid materials with polymeric amines and their CO_2 capture action.

Amine-functionalized solid adsorbents have attracted considerable attention as a hybrid solution that combines the advantages of aqueous amines and porous solids[4]. These materials are prepared by incorporating amines, either as small molecules or polymers, into solid supports via impregnation, grafting to, or in situ polymerization[10]. Among these, polymeric amines—polymers bearing amine groups in their backbone or side chains—stand out for their high amine density[11]. As shown in Figure 1.1, the integration of polyamines into porous matrices enables efficient CO_2 capture under both dry and humid conditions[12]. Compared to aqueous amine systems, these solid-supported amine adsorbents reduce energy consumption during regeneration and eliminate corrosion issues due to the existence of solid porous supports.

One of the most extensively studied porous supports for such applications is MCM-41, a mesoporous material with a high surface area and narrow pore size distribution[2]. Despite its popularity, as a result of the extremely small wall thickness,

MCM-41 suffers from poor hydrothermal stability at elevated temperatures[13], which severely limits its performance in practical post-combustion CO_2 capture processes. Notably, many commercial CO_2 capture systems require adsorbents to undergo periodic water-based washing steps, to remove contaminants, dissolve residual CO_2, or assist in thermal regeneration under humid conditions. Unfortunately, the framework of MCM-41 collapses under such hydrothermal treatment, resulting in loss of porosity and adsorption capacity[13]. Therefore, there is a critical need to develop adsorbent systems that retain the favorable properties of MCM-41, such as tunable mesopores and high surface area, while offering improved resistance to hydrothermal degradation.

To meet these challenges, recent advances in nanostructured material design have highlighted the potential of porous structures derived from block copolymer (BCP) self-assembly (SA). Mesoporous materials structure directed by BCP SA have emerged as a powerful tool for constructing nanoporous frameworks with controlled pore geometry and periodicity[14]. These BCPs, composed of covalently bonded yet chemically incompatible polymer blocks, spontaneously organize into ordered nanoscopic domains, yielding structures with characteristic dimensions typically of order tens of nanometers. The incorporation of selective additives—ranging from organic resols to inorganic sol–gel precursors—into a hydrophilic block of an amphiphilic BCP enables the generation of diverse hybrid morphologies. Effective structure direction requires favorable interactions between the additive and a specific polymer block, such as hydrogen bonding and/or dipolar interactions, and a suitable size match to ensure thermodynamic compatibility and confinement specifically to the hydrophilic block of the BCP[15]. Upon removal of the polymeric frameworks via thermal

treatments, the resulting inorganic materials can retain periodic mesoscale order and adopt functional compositions including oxides, carbons, and even superconducting materials. For instance, Beaucage et al.[16] demonstrated a synthesis route where a triblock terpolymer – poly(isoprene-*block*-styrene-*block*-ethylene oxide) (PI-*b*-PS-*b*-PEO or simply ISO) directed the assembly of niobium oxide into alternating gyroid networks. Through a combination of calcination, nitridation under ammonia, or carburization under various gaseous atmospheres, they produced mesoporous niobium nitrides and carbonitrides with exceptional structural stability at high temperatures.

While nanostructured porous materials offer high surface areas, they often exhibit transport limitations, especially at high rates. Limited transport through small pores therefore often restricts their practical performance. Nature overcomes this problem by employing asymmetric structures—as found, e.g., in lungs, blood vessels, and tree roots—that combine fast transport kinetics via wide transport channels on one side with high surface areas on the other[17]. For instance, the human respiratory system features a highly asymmetric architecture in which rapid convective airflow through large diameter trachea and bronchi is followed by diffusive transport in nanoscopic alveoli structures, enabling both rapid transport and extensive surface area for gas exchange[18]. Inspired by such biological systems, polymer membranes have been designed integrating BCP SA with non-solvent induced phase separation (NIPS) into the SNIPS (SA + NIPS) process, which integrates BCP SA with non-solvent induced phase separation (NIPS)[19]. NIPS yields asymmetric structures with low flow resistance, while BCP SA introduces a dense mesoporous top layer and walls with narrow pore size distribution. The resulting membrane features a hierarchical gradient—from dense, size-

controlled mesopores at the surface to increasingly larger pores at the base—achieving both high flux and high internal surface areas.

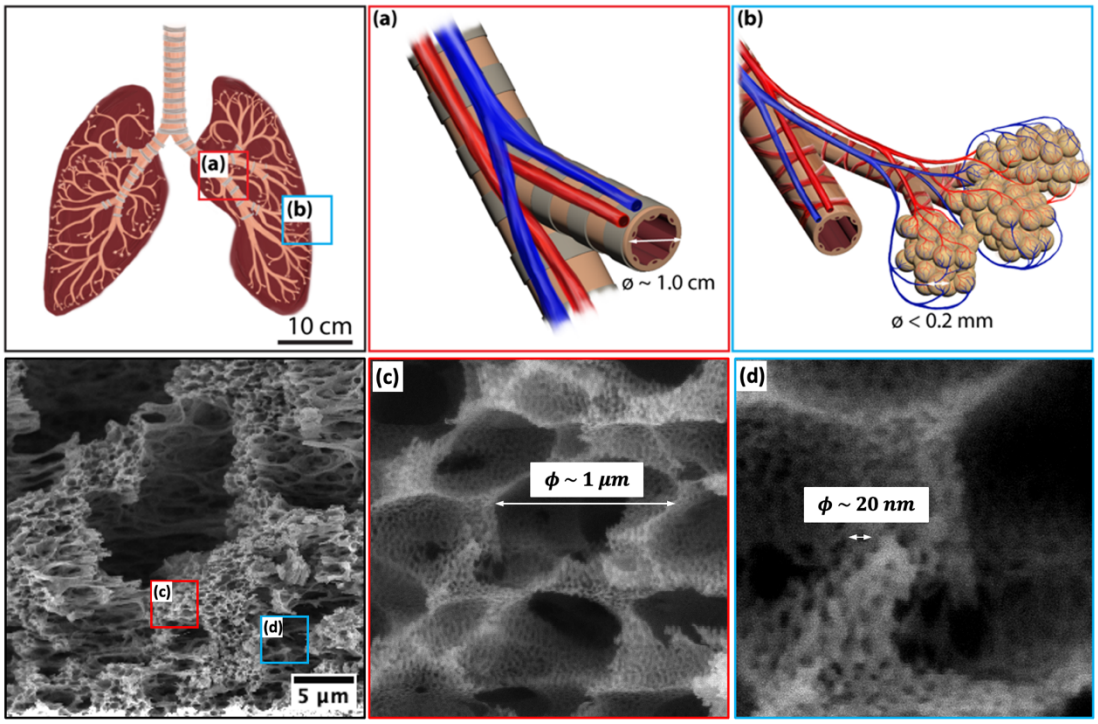

Figure 1.2. Asymmetric structure of the human respiratory system (top row)[17] compared to a designed asymmetric film derived from SNIPS (bottom row).

While originally developed for BCP based asymmetric membranes, the SNIPS process, like BCP SA, can be employed to guide the formation of asymmetric porous inorganic structures when additives are incorporated during membrane fabrication. In this strategy, the polymer and additive co-assemble into a hybrid asymmetric porous architecture, which is then subjected to thermal treatments to yield a range of inorganic materials[20]. The resulting freestanding porous structures (Figure 1.2 bottom row), retain the overall asymmetry of the original polymeric SNIPS-derived templates. The image in the Figure 1.2 (bottom row, left side) has been rotated— the bottom is pointing upward, and the mesoporous top surface is at the bottom—to visually highlight the analogy between this artificial membrane and the asymmetric organization found in the

human respiratory system. As illustrated in the schematic of the lung (top row in Figure 1.2), this organ exhibits a natural hierarchical structure: bronchi branch into narrower bronchioles, which ultimately terminate in nanoscopic alveoli with high surface area. Similarly in the designed system (bottom row in Figure 1.2), large macropores progressively decrease in size and transition into mesopores. The presence of large macropores facilitates high accessibility and convective flow, thereby enabling high flux. Furthermore, macropore walls are mesoporous, simultaneously providing large surface area through this structural hierarchy.

Compared with homogeneously mesoporous structures developed through BCP SA, the SNIPS-derived asymmetric architectures offer enhanced performance due to their combination of fast mass transport and high surface area. The combination of these structural advantages with the tunability and scalability of the SNIPS process makes such materials highly promising for applications in photocatalysis, energy conversion, and energy storage. Hesse et al.[18] demonstrated that such asymmetric structures, when converted into freestanding titanium nitride (TiN) and carbon membranes, exhibited both well-defined mesoporosity and hierarchical pore structures. This enabled ion transport at high-rates without sacrificing surface area in electrical double-layer capacitors (EDLCs). These materials achieved record power densities and competitive energy densities, overcoming the common trade-off between high-surface-area and high-flux requirements. In another study, Moore, Shoji et al.[21] applied SNIPS-derived asymmetric titanium dioxide (TiO_2) films as photocatalyst supports for low-temperature dry reforming of methane (DRM), achieving exceptionally high single-pass conversions and CO/H_2 production rates, particularly at high flow rates. Non-equilibrium derived

asymmetric SNIPS materials outperformed equilibrium BCP SA derived mesoporous control materials by orders of magnitude, even when the most open and accessible alternating gyroid morphology was employed. Their findings highlight how asymmetric pore structures enhance both surface accessibility and transport efficiency, ultimately driving catalytic performance beyond that of traditional mesoporous structures.

This present study introduces an asymmetric mesostructured TiO_2-based CO_2 adsorbent for comparison with homogeneous BCP equilibrium SA based materials to see whether advantageous observed in EDLCs and photocatalytic DRM also translate to CO_2 sequestration. If successful, because of the much larger wall thickness of BCP SA derived mesoporous materials, such asymmetric structures should also be able to address the hydrothermal instability limitations of conventional mesoporous materials such as MCM-41. The material is fabricated via a self-assembly and non-solvent induced phase separation (SNIPS) strategy using triblock terpolymer poly(isoprene-*block*-styrene-*block*-4-vinylpyridine) (PI-*b*-PS-*b*-P4VP, or simply ISV) as a structure-directing agent, combined with sol–gel-derived TiO_2 nanoparticles[18]. Subsequent calcination yields hierarchically porous TiO_2 films with an asymmetric pore structure, which are then impregnated with poly(ethylenimine) (PEI) to introduce chemisorptive amine sites. For comparison, alternating gyroidal TiO_2 with homogeneous and continuous mesoporosity is fabricated using evaporation-induced self-assembly (EISA) of the same inorganic precursor with triblock terpolymer ISO as structure directing agent[18].

Thermogravimetric analysis (TGA) is utilized to characterize the CO_2 capture performance of these porous materials by systematically investigating how parameters

such as PEI loading and structural asymmetry, adsorption temperature, CO_2 concentration, and flow rate influence CO_2 capture performance. Kinetic modeling is finally used to study multistage adsorption behaviors of the fabricated adsorbents. Importantly, the asymmetric architecture consistently outperforms gyroidal controls for a range of conditions tested. This suggests that the balance of rapid mass transport and high surface area enabled by such asymmetric structures is also advantageous for CO_2 sequestration. These results may provide valuable guidance for the design of scalable, regenerable, and hydrothermally stable adsorbents suitable for post-combustion CO_2 capture.

CHAPTER 2

EXPERIMENTAL SECTION

2.1 Materials Preparation

2.1.1 Materials

Materials were used as received except as otherwise indicated. The following chemicals were used for hybrid membrane fabrication: tetrahydrofuran (THF) (Sigma-Aldrich, anhydrous, ≥ 99.9 %, inhibitor-free), 1,4-dioxane (DOX) (Sigma-Aldrich, ACS reagent, ≥ 99.0%), titanium(IV) isopropoxide (Sigma-Aldrich, 99.999 % trace metals basis), hydrochloric acid (HCl) (VWR, ACS Grade, 36.5 % to 38 %), and deionized (DI) water with a resistivity of 18.2 MΩ·cm which was used as the non-solvent precipitation bath.

The following chemicals were used for amine impregnation: poly(ethylenimine) (PEI) (Sigma-Aldrich, average M_w ~25,000 by LS, average M_n ~10,000 by GPC, branched), methanol (MeOH) (Sigma-Aldrich, ACS reagent, ≥ 99.8%).

2.1.2 Amine-Impregnated Asymmetric TiO_2 Film Preparation

The poly(isoprene-*block*-styrene-*block*-4-vinylpyridine) (ISV) triblock terpolymer employed in this work was synthesized via sequential living anionic polymerization following a previously reported procedure[22]. The resulting polymer had a molar mass of 126 kg mol^{-1}, consisting of 27 vol% poly(isoprene) (PI), 64 vol% poly(styrene) (PS), and 9 vol% poly(4-vinylpyridine) (P4VP), with a dispersity (Đ) of 1.19. The volume fractions of the individual blocks were determined by proton nuclear

magnetic resonance spectroscopy (^{1}H NMR) in solution. Gel permeation chromatograph (GPC) was used to analyze the polymer's dispersity The total molar mass of ISV was calculated by combining the GPC-determined PI block mass with the NMR-derived block composition ratios.

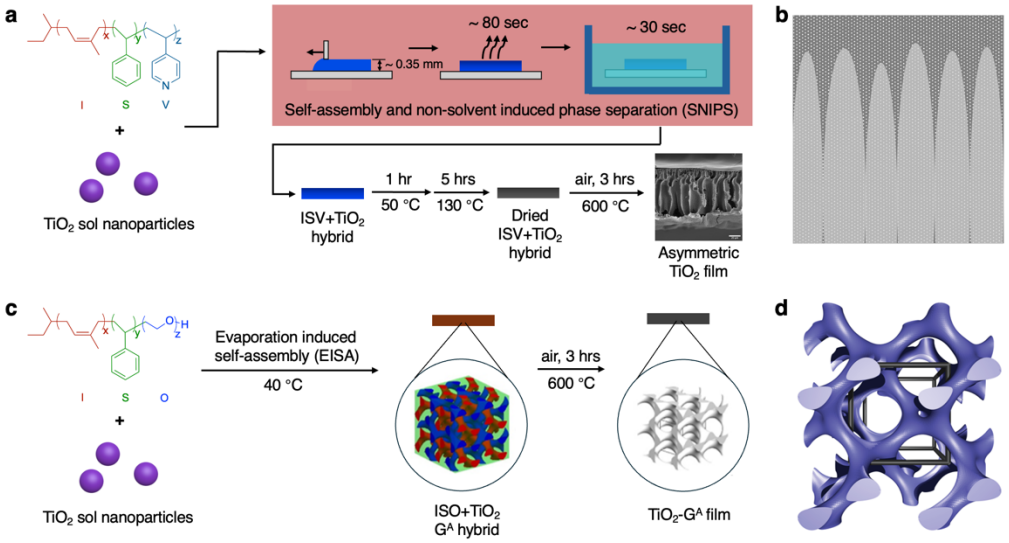

Figure 2.1. Schematic of the synthesis steps for ISV SNIPS-derived asymmetric TiO_2 (a) and ISO SA derived TiO_2-G^A (c). Illustrations of the asymmetric (b) and the G^A (d) support structures.

Figure 2.1 outlines the preparation procedure. The synthesized ISV was first dissolved in a 7:3 (mass ratio) mixture of DOX and THF at a polymer mass fraction of 15%, and the solution was stirred for 2 h to make a homogeneous solution. The TiO_2 sol nanoparticles were prepared separately via a hydrolytic sol–gel method, as previously reported[18]. Specifically, 1.0 mL of titanium(IV) isopropoxide was added to 0.3 mL of HCl in a septum-sealed vial and stirred vigorously for 5 min. Subsequently, 2.0 mL of THF was introduced into the mixture, which was then stirred for another 5 min. This freshly prepared sol was immediately added to the ISV solution. The resulting dope, containing an overall TiO_2 + ISV volume fraction of 7.9% in solvent, was stirred overnight to ensure complete mixing prior to casting.

ISV-TiO_2 hybrid membranes were fabricated via the SNIPS process. To that end, the prepared casting solution was pipetted onto a glass slide and subsequently cast into thin films using an automated blade-casting machine, with the gate height set between 305 µm and 381 µm. The thin films were left to evaporate for 80 s to establish a concentration gradient along the film normal. Immediately afterward, the films were immersed in a non-solvent DI water bath for 30 s to induce polymer precipitation and kinetically trap the resulting asymmetric pore structure. All casting procedures were carried out in a dry box maintained at room temperature, with relative humidity adjusted to 40–45% prior to casting[18].

The hybrid membranes were dried in vacuum, initially at 50 °C for 1 h, followed by 130 °C for an additional 5 h. This was followed by a calcination step in a box furnace under ambient air to remove the organic component and yield the freestanding TiO_2. The membranes were heated at a ramp rate of 1 °C min^{-1} to 600 °C, held isothermally at that temperature for 3 h, and then allowed to cool to room temperature.

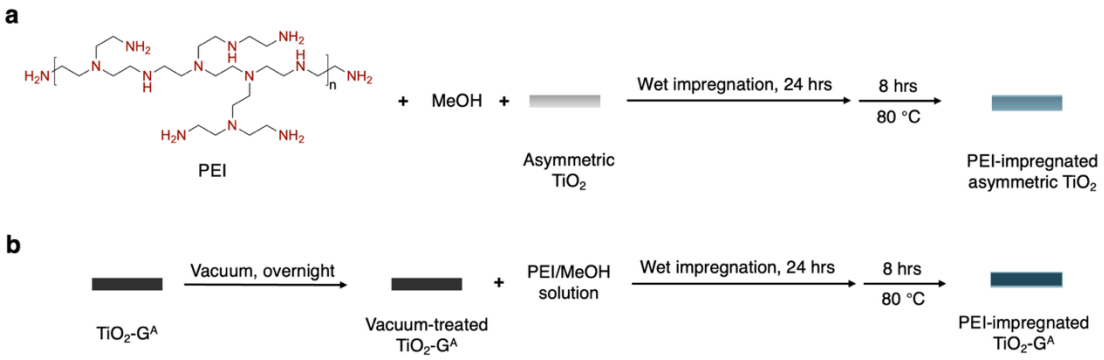

Figure 2.2. Schematic of the PEI impregnation steps for asymmetric TiO_2 (a) and TiO_2-G^A (b).

Amine impregnation was conducted using the wet impregnation method,[2] shown in panel (a) of Figure 2.2. PEI was first dissolved in MeOH under stirring for 15 min to

prepare a stock solution with a concentration of 50 mg/mL. A 6 mL aliquot of PEI/MeOH solution at the desired concentration was obtained by diluting this stock solution. Approximately 4 mg of the calcined TiO_2 films were added into 6 mL PEI/MeOH solution in a vial. The vial was then placed on a shaker and agitated at 100 rpm at room temperature for 24 h to allow for thorough impregnation. Afterward, the samples were dried in a vacuum oven at 80 °C for 8 h to ensure complete solvent removal.

2.1.3 Amine-Impregnated Alternating Gyroidal TiO_2 Film Preparation

The poly(isoprene-*block*-styrene-*block*-ethylene oxide) (ISO) triblock terpolymer, used for fabricating the BCP SA derived mesoporous materials as the controls, was synthesized via a previously reported sequential living anionic polymerization route[23]. The resulting polymer exhibited a molar mass of 83 kg mol^{-1}, consisting of 29 vol% poly(isoprene) (PI), 64 vol% poly(styrene) (PS), and 6.5 vol% poly(ethylene oxide) (PEO), with a polydispersity of 1.09, as characterized by a combination of ^1H NMR and GPC, following the same procedures used for ISV characterization.

The preparation of the alternating gyroidal TiO_2 materials followed a previously reported method[18], as illustrated in panel (c) of Figure 2.1. The ISO was dissolved in THF at a concentration of 25 mg/mL. The TiO_2 sol solution, synthesized as described above, was subsequently added to the polymer solution to achieve an overall TiO_2 + PEO volume fraction of 17.0%. The resulting mixture was stirred overnight before further processing.

To prepare the hybrid ISV+TiO_2 film, the casting solution was poured into a Teflon dish with a diameter of 1.5 inch, which was placed on a glass substrate and covered with a glass dome. The setup was maintained at 40 °C on a hot plate to allow for slow solvent evaporation. This evaporation-induced self-assembly (EISA) process was carried out overnight to promote the formation of a periodically ordered hybrid structure.

The resulting hybrid films were first heat-treated at 130 °C under vacuum, followed by CF_4 plasma etching on both sides at 300 W for 30 min to remove surface overlayers and ensure open pore accessibility from both the top and bottom surfaces. The subsequent calcination was carried out following the same protocol as previously described.

The impregnation process of the mesoporous TiO_2 films was conducted using a similar procedure to that applied for the asymmetric TiO_2 films, shown in panel (b) of Figure 2.2. However, prior to impregnation, the vials containing the calcined films were subjected to vacuum overnight at 40 °C to facilitate PEI infiltration by removing trapped air from the mesoporous structure. Following the overnight vacuum treatment, PEI/MeOH solution was then added into the vials. The subsequent shaking and drying steps were performed in the same way and under the same conditions as described for the asymmetric materials.

2.2 Materials Characterization

2.2.1 Scanning electron microscopy (SEM)

Scanning electron microscopy (SEM) micrographs were obtained using a Tescan Mira3 field emission scanning electron microscope (FESEM), equipped with an in-lens detector, at an accelerating voltage of 5 kV. All asymmetric membrane and film samples were sputter-coated with gold-palladium using a Denton Vacuum Desk II prior to SEM imaging. SEM images were brightness/contrast adjusted using ImageJ, and scale bars were added.

2.2.2 Nitrogen Sorption

Nitrogen adsorption-desorption isotherms were recorded using a Micromeritics ® ASAP 2020 surface area and porosity analyzer at -196 ℃. TiO_2 films were loaded into a quartz glass tube, then degassed at 120°C under high vacuum overnight. The degassed sample and tube were then attached to the analysis port of the instrument, immersed in liquid nitrogen, and analyzed. The specific surface areas were determined using the Brunauer-Emmett-Teller (BET) method[24,25]. The pore size distributions were obtained using the Barrett-Joyner-Halenda (BJH) analysis of the desorption branches[26].

2.2.3 Thermogravimetric Analysis (TGA)

Thermogravimetric measurements were performed using a TA Instruments TGA 5500. TGA was employed to determine both the mass of PEI loading and the CO_2 adsorption capacity of the PEI-impregnated TiO_2 samples.

For PEI loading quantification, the samples were placed in platinum pans and heated under an air flow of 10 mL/min. The temperature was increased from room temperature to 600 °C at a ramp rate of 5 °C min^{-1}, followed by natural cooling to room

temperature. A small mass loss observed around 100 °C was mainly attributed to the desorption of adsorbed CO_2 and moisture[27]. The actual PEI content was determined from the mass loss occurring between 100 °C and 600 °C.

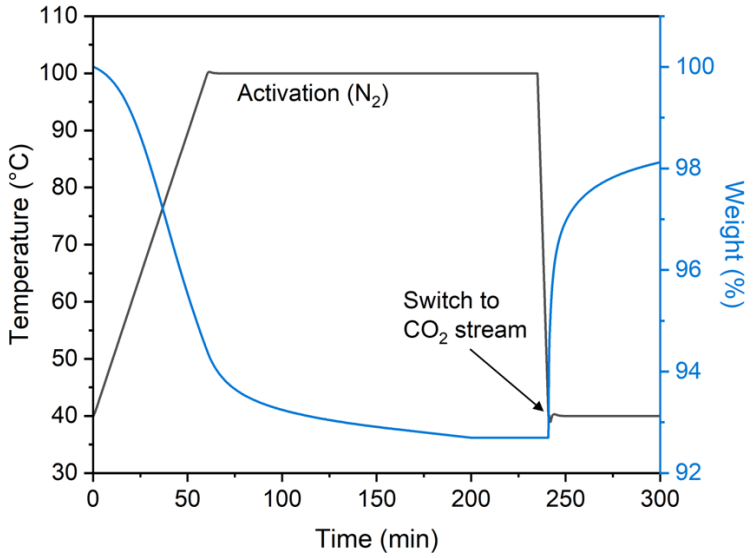

Figure 2.3. Overview of TGA adsorption kinetics assay. The sample is first activated under flowing N_2, followed by a temperature adjustment under the same atmosphere. The gas flow is then switched to a CO_2-containing stream.

In CO_2 adsorption experiments (Figure 2.3), samples were first activated under flowing N_2 at 60 mL/min and 100 °C for a sufficient duration, typically until the mass stabilized, ensuring the removal of adsorbed gases and moisture. The system was then adjusted to the target adsorption temperature, allowed to equilibrate, and the gas flow was switched to a CO_2-containing stream. The sample was held isothermally under this stream until a new mass plateau was reached. After each measurement, the sample was reactivated under N_2 and subjected to the next experimental condition (e.g., different adsorption temperature, CO_2 concentration, or flow rate). To ensure consistency, the same physical sample was used for all comparative measurements across different conditions, remaining in the TGA furnace. The CO_2 uptake for each condition was

determined from the net mass increase during exposure to the CO_2-containing gas stream.

2.2.4 Small-Angle and Wide-Angel X-Ray Scattering (SAXS and WAXS)

Small-angle and wide-angle X-ray scattering (SAXS and WAXS) were performed on pieces broken from film samples at the Soft Matter Interfaces (SMI, 12-ID) beamline at the National Synchrotron Light Source II (NSLS-II). At SMI, the X-ray energy was 16.1 keV. The SAXS detector was a Pilatus 1M pixel array detector at a distance of 5.00 m from the sample. The WAXS detector was a Pilatus 900KW pixel array detector. Two-dimensional (2D) scattering signals collected at various detector positions were stitched together to construct the WAXS scattering profiles over the entire q (scattering vector) range. All the 2D raw scattering data were processed and azimuthally integrated using custom-generated software packages at the beamline.

CHAPTER 3

RESULTS AND DISCUSSION

3.1 Fabrication and Amine Functionalization of TiO_2 Films

3.1.1 Morphological Optimization of Asymmetric TiO_2 Films

Panel (a) in Figure 3.1 shows characterization results of a typical asymmetric TiO_2 film that was subsequently used for PEI impregnation using SEM. Three SEM images are shown. From top to bottom, they exhibit the top surface layer, the film cross section, and the bottom surface layer. Overall, the film exhibits an asymmetric, hierarchical pore structure with the cross-sectional view showing so-called finger-like pores extending approximately 100 μm in thickness from the bottom of the film almost all the way to the top surface layer. The walls and top surface layer exhibit well-defined mesoporosity throughout. The top surface shows a mesoporous layer about 100 nm thick, with relatively uniform mesopore sizes. Beneath this top layer lies the asymmetric, finger-like substructure with macropore size increasing progressively with depth. The walls of the macropores are mesoporous as demonstrated in the inset of the cross-sectional view. The bottom surface of the film shows macropores with diameters on the order of 1 μm. This pore morphology combines a large specific surface area from the mesopores, advantageous for applications as separation membranes[28] or for surface catalysis[21], with fast mass transport enabled by the finger-like structure and the large open pores at the film bottom. These structural characteristics are expected to influence the CO_2 adsorption behavior, which will be discussed in more detail in the following sections.

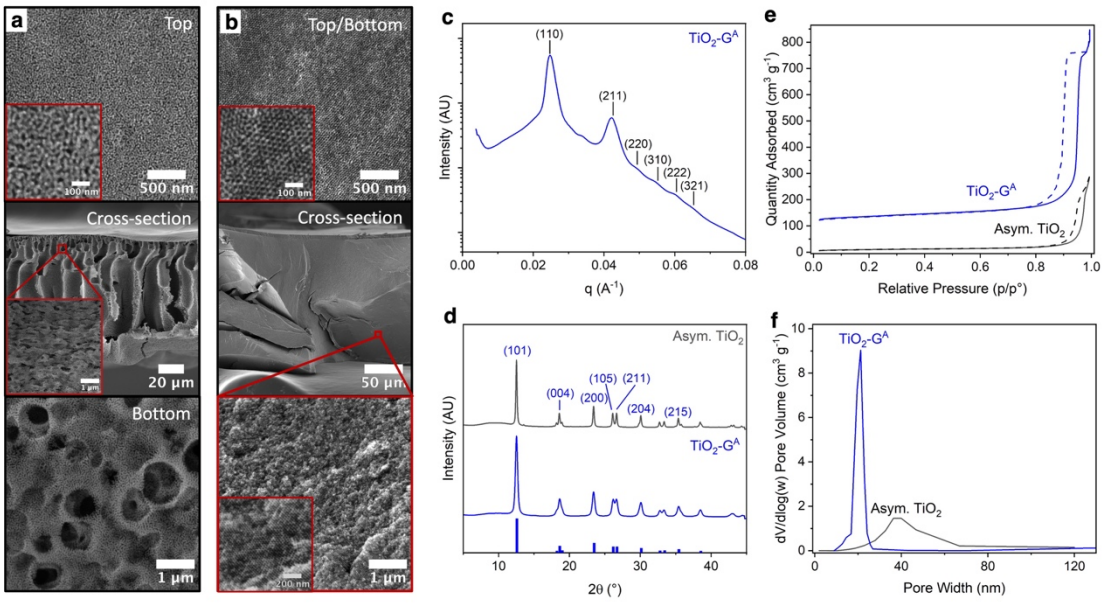

Figure 3.1. Characterization of asymmetric TiO_2 and alternating gyroidal (G^A) TiO_2. (a) SEM characterization of asymmetric TiO_2, from top to bottom: top surface, asymmetric cross-section, and macroporous bottom surface. (b) SEM characterization of TiO_2-G^A. Surface (top) and cross-section (bottom) images are shown for each sample. As the G^A sample is homogeneous, the surface image is representative for both top and bottom surfaces. Insets in (a) and (b) show magnified views to better visualize structural features. (c) SAXS results for TiO_2-G^A. Visible peaks are indexed according to expected peak positions for a G^A lattice, as indicated. (d) WAXS results of asymmetric TiO_2 (black) and TiO_2-G^A (blue) materials. Blue tick marks correspond to the expected peak positions and relative intensities of a tetragonal crystal system of anatase TiO_2. (e) Nitrogen sorption/desorption isotherms of asymmetric TiO_2 (black) and TiO_2-G^A (blue) materials. (f) BJH-derived pore size distributions of asymmetric TiO_2 (black) and TiO_2-G^A (blue) materials.

The asymmetric TiO_2 film shown in panel (a) of Figure 3.1 was prepared under optimized conditions: ISV was dissolved in a THF/DOX (3:7, w/w) solvent mixture at a polymer concentration of 15 wt.%. After the addition of TiO_2 sol nanoparticles, the resulting dope solution was cast into a membrane and allowed to evaporate for 80 s before being immersed in DI water for precipitation. To find these optimal processing parameters, both polymer concentration and evaporation time were varied.

In terms of evaporation time, both 60 s and 80 s were tested. Even longer evaporation times were avoided because they are known to promote a transition from a finger-like substructure to a sponge-like one. The latter is less favorable for improving

mass transport across the membrane as compared to finger-like substructure[20]. As shown in Figure A.1, increasing the evaporation time from 60 to 80 s led to a more uniform mesopore distribution and better-defined pore sizes across all tested polymer concentrations. This improvement can be attributed to more extensive solvent evaporation, which increases the local polymer concentration at the film surface and promotes more regular micelle formation and arrangement. These micellar structures were then preserved in place during the non-solvent-induced phase separation step. Even after removal of the polymer matrix by calcination, the resulting inorganic TiO_2 network preserved the original pore ordering.

Similarly, increasing the polymer concentration in the dope solution also resulted in a more ordered top-surface pore morphology. However, if the concentration was chosen to be too high, the solution became too viscous, which slowed down micelle movement, ultimately preventing long-range ordering due to kinetic limitations consistent with previous studies on SNIPS membranes[20]. Based on these tests, a polymer concentration of 15 wt.% and an evaporation time of 80 s were selected as the optimal conditions for preparing asymmetric TiO_2 films. Unless otherwise mentioned, all asymmetric TiO_2 samples discussed in this work were prepared under these conditions.

3.1.2 Controlled Amine Impregnation of Asymmetric TiO_2 Films

After successfully optimizing the protocols for asymmetric TiO_2 film formation to be employed as a support for CO_2 adsorbents, the films were immersed in PEI/MeOH solutions to allow PEI to diffuse into the porous network. PEI macromolecules are

expected to adhere via hydrogen bonding to the outer surface of the TiO_2 films as well as to the internal surfaces of the hierarchically organized pores, resulting in the formation of a continuous PEI layer. In this study, the amount of PEI loading on the TiO_2 support was controlled by adjusting the concentration of the PEI/MeOH solution, which in turn determined the thickness of the PEI layer.

Figure A.2 shows SEM images of the top surface, cross-section, and bottom surface of asymmetric TiO_2 films after immersion for 24 h in PEI/MeOH solutions with different concentrations. As the solution concentration increased, sizes of the mesopores observed on both the top and bottom surfaces, as well as within pores seen in cross-sectional images, progressively decreased, suggesting thicker PEI surface layer formation. When the PEI concentration reached 25 mg/mL, the mesopores on top surfaces were almost completely closed by the deposited PEI.

To further confirm and quantify the extent of PEI impregnation into the TiO_2 support, thermogravimetric analysis (TGA) was employed. TGA, which measures the weight change of a material as a function of temperature or time, was used to quantify the PEI loading. To that end, in this study samples were heated to 600 °C at a ramp rate of 5 °C/min.

Results of TGA experiments using these conditions for untreated asymmetric TiO_2, amine-impregnated TiO_2 prepared from PEI/MeOH solutions of different concentrations, and pure PEI are shown in Figure A.3. As expected, the pure asymmetric TiO_2 showed almost no weight loss up to 600 °C. For pure PEI, a first weight loss was observed below ~75 °C, which is attributed to the desorption of moisture and CO_2 adsorbed by the amine groups[27]. After a stable region between ~75-150 °C, PEI

decomposition began above 150 °C. Beyond ~175-200 °C, the decomposition entered a second stage where the rate of weight loss slightly decreased compared to the initial stage. Reaching 530 °C, PEI was fully decomposed and volatilized. For decreasing amounts of PEI impregnated into the asymmetric TiO_2, the distinction between these two decomposition stages (below and above 175-200 °C) became increasingly less pronounced and decomposition leveled off at lower and lower temperatures. Completion of the decomposition process at lower and lower temperatures suggested that the TiO_2 support increasingly destabilized the PEI films with decreasing film thickness, consistent with expectations of the self-cleaning properties of TiO_2 nanomaterials[29].

The weight loss between 100 °C and 600 °C was solely attributed to the decomposition of PEI and was therefore used to estimate the PEI loading in the samples. Based on this method, the PEI loadings for asymmetric TiO_2 films treated with 5, 6.5, 10, and 25 mg/mL PEI/MeOH solutions were determined to be approximately 15, 20, 30, and 45 wt.%, respectively.

3.1.3 Fabrication and Structural Analysis of Mesoporous TiO_2 Films with Alternating Gyroid Morphology

As a control group to the asymmetric TiO_2 films, homogeneously structured mesoporous TiO_2 films with alternating gyroid morphology (TiO_2-G^A) were prepared following a previously reported method[18]. To that end, a hybrid precursor solution was obtained by mixing ISO with TiO_2 sol nanoparticles. Structure formation occurred overnight via evaporation-induced self-assembly (EISA) at 40 °C, leading to the

development of a gyroidal morphology. The resulting hybrid ISO/TiO_2 films were then heat-treated under vacuum at 130 °C for 5 hours, followed by calcination in air to remove the polymer matrix and crystallize the inorganic TiO_2 network. Panel (b) in Figure 3.1 presents SEM images of a TiO_2-G^A sample, clearly showing periodically ordered mesopores on both the top and bottom surfaces (see inset in the top panel) as well as a continuous interconnected periodically ordered pore network visible in the cross-sectional image (see inset in the bottom panel).

In addition to SEM, small-angle X-ray scattering (SAXS) was used to characterize the structure of the TiO_2-G^A films. SAXS was not applied to the asymmetric TiO_2 due to the lack of periodic mesoscale order in this material. The SAXS pattern of TiO_2-G^A is shown in panel (c) of Figure 3.1, with tentative peak assignments consistent with an alternating gyroid lattice with a cubic lattice unit cell parameter of 35.9 nm.

3.1.4 Overcoming Diffusion Limitations in TiO_2-G^A Films via Vacuum Treatment

To prepare the amine-impregnated TiO_2-G^A samples, the same impregnation procedure as used for the asymmetric TiO_2 films was initially applied. However, this method proved less effective for the TiO_2-G^A. When low concentrations of PEI/MeOH solution (5 and 10 mg/mL) were used, the resulting PEI loadings were significantly lower than those obtained for asymmetric TiO_2 films under the same conditions. Moreover, an additional issue emerged when the concentration of the amine solution was further increased (e.g., to 25 mg/mL). As shown in panel (a) of Figure A.4, under these conditions the mesopores on the top and bottom surfaces became clogged with

PEI, while cross-sectional SEM images still exhibited a well-defined mesoporous structure. This suggested that PEI tends to accumulate at or near the external surfaces, blocking the entrance of the mesopores and inhibiting deep infiltration of PEI into the interior of the monolithic material with gyroidal network structure.

To address this issue, alternative strategies were explored, including extending the impregnation duration, performing multiple impregnation cycles with dilute PEI solutions, pre-soaking the samples in pure MeOH followed by centrifugation, and applying vacuum treatment prior to impregnation. Among these, the most effective approach was the vacuum pre-treatment. To that end, approximately 4 mg of TiO_2-G^A sample was placed in a septum-sealed vial and heated on a hot plate at 40 °C. A thin tube was used to connect the vial to a vacuum line, and the sample was left under vacuum overnight. Following the overnight degassing step, 6 mL of PEI/MeOH solution was taken up using a syringe and injected into the vial through the septum. The vial containing both the TiO_2-G^A sample and PEI/MeOH solution was then placed on a shaker and agitated at 100 rpm at room temperature for 24 h.

After vacuum treatment, PEI could more effectively infiltrate the interconnected mesoporous network and adhere to the internal surfaces. This was likely due to the removal of trapped air inside the pore volume of the monoliths, significantly enhancing the accessibility of the interior pore volume of the TiO_2-G^A sample. As shown in panel (b) in Figure A.4, when impregnated with the same 25 mg/mL PEI/MeOH solution, the vacuum-treated sample now retained open pores on the external surfaces, in contrast to the clogging observed in untreated samples shown in panel (a) of Figure A.4. Furthermore, in cross-sectional SEM image, the mesostructure appeared less defined,

suggesting successful PEI infiltration into the internal pore volume of the sample. Compared to the untreated sample, the PEI distribution after vacuum treatment was more uniform, with deeper penetration into the interior while preserving open surface porosity, thus improving both internal utilization and overall accessibility.

After confirming that the vacuum pre-treatment enabled successful preparation of amine-impregnated TiO_2-G^A samples, the PEI loading was tuned by varying the concentration of the PEI/MeOH solution. Figure A.5 shows the surfaces and cross-sections of TiO_2-G^A after immersion in PEI/MeOH solutions of 5, 10, 25, and 50 mg/mL for 24 h. Across all concentrations, the surface pores remained open. The cross-sectional images capture regions near the sample surface. As the PEI concentration increased, the mesoporous network appeared progressively less well-defined, which could be attributed to increased PEI deposition within the mesopores. The feature size showed a slight increase, accompanied by thickened pore walls and blurred contrast between adjacent pores, suggesting partial infilling of the internal mesoporous structure by PEI. TGA was subsequently used to quantify the amount of PEI incorporated in the samples, as shown in Figure A.6. The PEI loadings for TiO_2-G^A samples treated with 5, 10, 25, and 50 mg/mL PEI/MeOH solutions were approximately 9, 15, 17, and 20 wt.%, respectively. For consistency and comparison, pure TiO_2-G^A without amine impregnation was also included in the analysis. These findings confirmed that vacuum-assisted PEI impregnation yielded tunable loadings and preserved mesopore accessibility in TiO_2-G^A samples.

3.1.5 Comparative Structural Characterization of Asymmetric TiO_2 and TiO_2-G^A Films

In addition to SEM and TGA, wide-angle X-ray scattering (WAXS) and nitrogen sorption measurements were employed to characterize both asymmetric TiO_2 and TiO_2-G^A. The WAXS patterns of both samples in panel (d) of Figure 3.1 exhibited diffraction peaks corresponding to the tetragonal anatase phase of TiO_2, indicating that thermal treatment at 600 °C induced crystallization of the oxide framework.

Table 3.1. Summary of Structural Characterization Results for TiO_2 Supports.

Material	Trace color	BET surface area ($m^2\ g^{-1}$)	Average pore width (nm)	Single point adsorption pore volume ($cm^3\ g^{-1}$)	Porosity (%)
Asymmetric TiO_2	Black	36.7	38.1	0.427	64.4
TiO_2-G^A	Blue	130	21.2	1.09	82.2

Nitrogen sorption isotherms (panel e in Figure 3.1) of both samples displayed type-IV curves with H1-type hysteresis and a sharp capillary condensation step near $P/P^0 \approx 0.99$, typical of mesoporous materials. Brunauer-Emmett-Teller (BET) method derived surface areas, pore volumes, and porosities are summarized in Table 3.1 (Methods).[24,25] According to Barrett-Joyner-Halenda (BJH) analysis of the desorption branches (Methods, panel f in Figure 3.1),[26] asymmetric TiO_2 exhibited a broad pore size distribution centered at 36–40 nm, while TiO_2-G^A showed a narrower distribution peaking at ~21 nm.

From similar analyses, the pore size of TiO_2-G^A was smaller than that of asymmetric TiO_2, while its surface area was significantly larger than that of asymmetric TiO_2. This contrast reflects the differences in the structures: TiO_2-G^A features a co-continuous and periodic gyroidal network, while the asymmetric TiO_2 displays a highly

asymmetric, hierarchical pore morphology with mesopores confined to the walls of the macropores.

3.1.6 Practical Advantages of Working with Asymmetric TiO_2 Relative to TiO_2-G^A Films

Compared to TiO_2-G^A samples, asymmetric TiO_2 films offered several practical advantages. First, the TiO_2-G^A samples required an additional vacuum pre-treatment step during PEI impregnation to achieve relatively uniform and high loadings resulting in open pore access. This added step increased the complexity of the process and presented scalability challenges, as implementing vacuum treatments on an industrial scale is both technically demanding and costly. In contrast, asymmetric TiO_2 films did not require this extra step to achieve high uniform loadings and open pore access. In fact, applying the same vacuum pre-treatment to asymmetric TiO_2 films showed negligible improvements in PEI loading, as demonstrated by the TGA results in Figure A.7. These results suggested that the asymmetric film architecture inherently facilitates efficient amine impregnation relative to equilibrium derived mesoporous films, highlighting a substantial advantage of this structure.

Second, achieving equivalent PEI loadings required substantially more concentrated PEI/MeOH solutions for TiO_2-G^A than for asymmetric TiO_2 films. For instance, to reach a PEI loading of 20 wt.%, the gyroidal sample required a 50 mg/mL PEI solution, while the asymmetric sample only needed a PEI concentration of 6.5 mg/mL, i.e., requiring less than one seventh of the polymer material. This implies

that the asymmetric structure provides significantly higher accessibility to PEI polymer, resulting in more efficient utilization of the amine and lower material costs.

Third, the asymmetric TiO_2 films offer better scalability for industrial-scale production. Derived from the widely used industrial NIPS process, the SNIPS method employed for asymmetric TiO_2 film formation is compatible with industrial roll-to-roll manufacturing[30]. By comparison, the formation of TiO_2-G^A films typically relies on the process of EISA, which requires precise environmental control and long processing times, limiting its feasibility for large-area or continuous manufacturing. Therefore, asymmetric TiO_2 films not only reduce material and energy input during amine functionalization but also align better with high-throughput production needs.

3.2 CO_2 Adsorption Behavior of PEI-Impregnated Block Copolymer Directed Asymmetric TiO_2

The CO_2 adsorption performance of amine-impregnated TiO_2 films was evaluated using TGA. The entire testing procedure can be divided into four segments. The first segment involved degassing the sample at the activation temperature under a nitrogen flow. Activation temperature refers to the temperature at which an adsorbent is heated to enhance its adsorption capacity by removing pre-adsorbed species. In this study, the activation temperature was set to 100 °C because, as discussed earlier and supported by the TGA profile of pure PEI shown in Figure A.3, both water and pre-adsorbed CO_2 could be removed at this temperature, while PEI remained thermally stable. The second segment involved equilibrating the sample at the target adsorption temperature. Once equilibrium was reached, the gas flow was switched from pure N_2 to

a CO_2-containing stream, initiating the adsorption process. During this stage, the sample mass increased over time until a plateau was reached, indicating that equilibrium CO_2 uptake had been achieved under the given conditions. Finally, in the desorption process, the gas flow was switched back to pure N_2 under the activation temperature. This enabled the desorption of CO_2 and the regeneration of the adsorbent. Ideally, after sufficient desorption time, the sample mass should return to its initial value prior to adsorption.

The CO_2 uptake for each condition was quantified from the measured weight change during the adsorption process. In this section, the systematic investigation of the effects of adsorption temperature, flow rate, CO_2 concentration, and PEI loading on the CO_2 adsorption performance of the amine-impregnated asymmetric TiO_2 films is discussed.

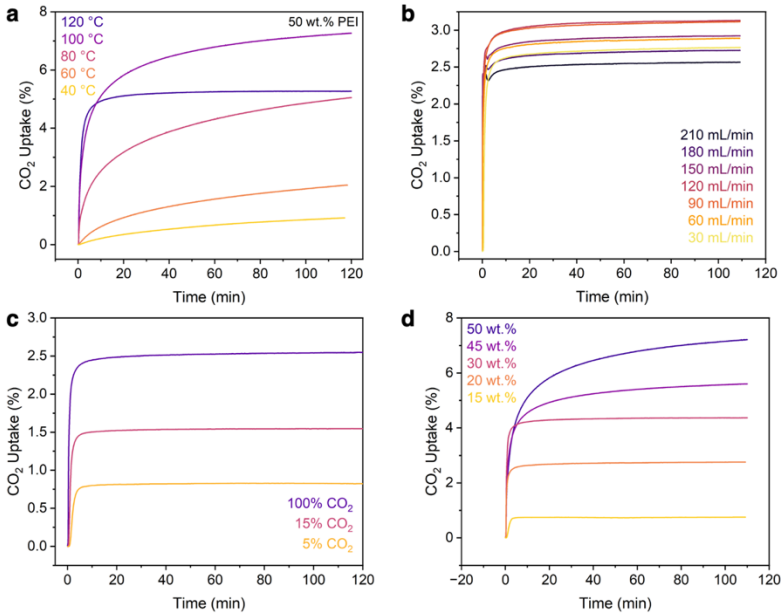

Figure 3.2. CO_2 adsorption profiles of PEI-impregnated asymmetric TiO_2 films under various operational conditions: (a) behavior of film loaded with 50 wt.% PEI at different temperatures in a 60 mL/min flow of pure CO_2 ; (b) behavior of film loaded with 20 wt.% PEI at different flow rates of pure CO_2 at 100 °C; (c) behavior of film loaded with 20 wt.% PEI in a 60 mL/min flow at 100 °C for different CO_2 concentrations; (d) behavior of films with different PEI loadings in a 60 mL/min pure CO_2 flow at 100 °C.

3.2.1 Effect of Adsorption Temperature

The influence of adsorption temperature was investigated under a pure CO_2 atmosphere with a fixed flow rate of 60 mL/min using asymmetric TiO_2 film samples impregnated with either 20 wt.% or 50 wt.% PEI. Panel (a) in Figure 3.2 shows the CO_2 adsorption profiles of samples with 50 wt.% PEI loading at various temperatures: 40, 60, 80, 100, and 120 °C, over a period of 2 h. Higher temperatures were not tested to avoid potential thermal decomposition of PEI. Among these tested conditions, only the curve at 120 °C reached a plateau within 2 h, indicating equilibrium CO_2 uptake. At all lower temperatures, even at the end of the two-hour period the adsorption profiles continued to rise, albeit slowly, suggesting that equilibrium had not yet been reached. Below 100 °C, CO_2 uptake after 2 h increased with increasing temperature. However, at 120 °C, the equilibrium uptake was lower than the 2 h uptake at 100 °C. This behavior can be explained by considering the dual contributions of physisorption and chemisorption in the amine-impregnated samples. Physisorption, governed by van der Waals (weak intermolecular) interactions, is exothermic and generally decreases with increasing temperature[31]. Chemisorption involves the formation of covalent bonds between CO_2 and the adsorbent[32]; in this system, PEI reacts with CO_2 to form carbamates (as illustrated in Figure 1.1), a process that is also exothermic. Therefore, elevated temperatures reduce the equilibrium capacity of the material due to the thermodynamic penalty on exothermic processes. On the other hand, low temperatures can hinder CO_2 diffusion and reduce the frequency of collisions between CO_2 molecules and active sites. Additionally, chemical adsorption requires overcoming an activation energy barrier, so moderate heating can promote the reaction kinetics. As a result, even

though equilibrium was not reached within 2 h, 100 °C emerged as the most favorable condition, achieving the highest CO_2 uptake in the temperature range tested. The effect of temperature on adsorption kinetics is also evident from the initial slope of the uptake curves. During the first five minutes, the profile at 120 °C exhibited the steepest rise, with lower temperatures showing progressively gentler initial slopes. This behavior is consistent with the thermally activated kinetics of chemisorption.

The CO_2 adsorption profiles of 20 wt.% PEI-impregnated samples in 60 mL/min pure CO_2 flow between 40 °C and 120 °C in steps of 20 °C for 3 h are shown in Figure A.8. From the shapes of the measured curves it can be concluded that the samples reached adsorption-desorption equilibrium for 80 °C and 100 °C. At 120 °C, the sample mass even exhibited a gradual decline over time, suggesting that the desorption rate exceeded the chemisorption rate for this elevated temperature, resulting in a net decrease in CO_2 uptake. In contrast, at 40 °C and 60 °C, the adsorption curves continued to rise slowly during the later stages of the process, indicating that equilibrium had not yet been reached. Notably, the slope of the 40 °C curve in the final stage was steeper, suggesting a stronger trend toward further CO_2 uptake. After 3 h of adsorption, the measured CO_2 uptake at 40 °C, 60 °C, and 80 °C was comparable and higher than that observed at 100 °C and 120 °C. However, the curve at 40 °C showed a more pronounced upward trend, suggesting that this temperature may yield the highest equilibrium uptake if the adsorption time were extended. Therefore, 40 °C was identified as the optimal adsorption temperature for samples with 20 wt.% PEI loading under the tested conditions. This optimal temperature differed significantly from that observed for samples with 50 wt.% PEI loading, where 100 °C provided the best performance. This

discrepancy can be attributed to differences in the spatial distribution of PEI within the asymmetric TiO_2 films at different loadings. At lower loadings (e.g., 20 wt.%), PEI tends to form a more dispersed, monolayer-like distribution, providing high exposure of amine active sites and facilitating CO_2 access. In contrast, at higher loadings (e.g., 50 wt.%), PEI forms a thicker layer on the support, which introduces significant diffusion resistance for CO_2 molecules. In such cases, a higher temperature is required to reduce the viscosity of PEI and enhance CO_2 diffusion through the polymer matrix.

Different types of CO_2 adsorbents typically operate within distinct temperature ranges. Among them, amine-functionalized solid adsorbents, such as PEI- or TEPA-loaded MCM-41, have been extensively studied and perform well between room temperature and 75 °C[33]. While their CO_2 uptake at 100 °C remains appreciable[34], adsorbents often require immersion in water during regeneration to dissolve carbamate species, which poses a challenge for MCM-41 due to its limited hydrothermal stability at elevated temperatures[13]. In contrast, 50 wt.% PEI-impregnated asymmetric TiO_2 films show optimal CO_2 adsorption at 100 °C. The TiO_2 framework retains its structure in boiling water, highlighting its superior thermal and hydrothermal stability[35]. This is particularly advantageous for real-world applications, as industrial exhaust streams, such as those from flue gas treatment and geothermal power plants, often operate between 90 and 150 °C. In such scenarios, cooling the gas to room temperature would be energy-intensive and economically inefficient. Therefore, PEI-impregnated asymmetric TiO_2 films, which offer both high CO_2 uptake and structural stability at 100 °C, have a distinct advantage over conventional amine-functionalized adsorbents.

Their robust performance under elevated temperatures makes them promising candidates for industrial CO_2 capture at moderate temperatures.

3.2.2 Effect of Flow Rate

The effect of gas flow rate was investigated using 20 wt.% PEI-impregnated asymmetric TiO_2 film samples at 100 °C under a pure CO_2 atmosphere, with results shown in panel (b) of Figure 3.2. When the flow rate was below 90 mL/min, the CO_2 uptake increased with rising flow rate. However, at flow rates above 120 mL/min, the uptake decreased as the flow rate increased. The CO_2 adsorption capacities at 90 mL/min and 120 mL/min were comparable, suggesting that the optimal flow rate range lay between 90 and 120 mL/min. This trend can be explained by considering both external mass transfer limitations and gas–solid contact time. At low flow rates, the thickening of the boundary layer leads to slower diffusion of CO_2 from the bulk gas to the adsorbent surface, resulting in reduced concentration gradients and weaker driving forces for adsorption. Consequently, the overall uptake rate slows down and more time is required to approach equilibrium. In contrast, excessively high flow rates cause the gas to pass through the adsorption bed too quickly, reducing the contact time between CO_2 molecules and active amine sites. As a result, some CO_2 molecules are unable to diffuse into the porous network or participate in chemical reactions, leading to lower uptake despite the fast flow.

The initial slopes of the uptake curves also provide insight into adsorption kinetics. Within the first five minutes, the initial adsorption rate increased with flow rate, especially up to 150 mL/min. This is attributed to enhanced mass transfer at higher flow

rates, which promotes steeper concentration gradients and accelerates delivery of CO_2 to the adsorbent surface. However, beyond 150 mL/min, the differences in initial slopes became marginal. Interestingly, a small but sharp dip in the apparent sample mass was observed at the beginning of the adsorption curves when the flow rate was ≥ 150 mL/min. This phenomenon is unlikely the result from actual desorption, as such a rapid mass loss is physically implausible. Instead, it is attributed to buoyancy effects triggered by the fast influx of cold gas into the furnace[36]. At high flow rates, this sudden introduction of cooler CO_2 gas causes localized temperature fluctuations, altering the gas density and temporarily increasing buoyant forces on the sample. As the gas environment stabilizes, the apparent mass recovers to a steady state.

3.2.3 Effect of CO_2 Concentration

Panel (c) in Figure 3.2 presents the CO_2 adsorption profiles of 20 wt.% PEI-impregnated asymmetric TiO_2 film samples at 100 °C under a flow rate of 60 mL/min of gas with varying CO_2 concentrations. A clear trend was observed: higher CO_2 concentrations led to faster initial adsorption rates, more complete uptake, and higher equilibrium adsorption capacities. This behavior can be explained by both kinetic and thermodynamic considerations. Kinetically, higher CO_2 concentrations increase the reactant availability, accelerating the formation of carbamate species between CO_2 and the amine groups on PEI. Simultaneously, the steeper concentration gradient enhances external mass transfer, facilitating faster transport of CO_2 molecules to the adsorbent surface and accelerating the overall adsorption process. From a thermodynamic perspective, increasing the CO_2 concentration shifts the adsorption equilibrium toward

product formation, in accordance with Le Chatelier's principle. This drives greater formation of carbamates and allows deeper penetration of CO_2 into the porous structure, effectively utilizing more of the available amine sites. As a result, both the rate and the extent of adsorption increased with CO_2 concentration, until saturation limits are approached.

It is worth noting that the 15 vol% CO_2 streams used here simulates the CO_2 concentration in flue gas from coal-fired power plants, while the 5 vol% stream corresponds to that from natural gas combined cycle (NGCC) systems. The fact that appreciable CO_2 capture was still observed even at 5 vol% indicates the capability of amine-impregnated asymmetric TiO_2 film adsorbents to function effectively across a broad range of emission sources with varying CO_2 concentrations.

3.2.4 Effect of PEI Loading

PEI loading is another critical factor influencing the CO_2 adsorption performance of amine-impregnated asymmetric TiO_2 films. Panel (d) in Figure 3.2 shows the adsorption profiles of samples with different PEI loadings under 100 °C and 60 mL/min pure CO_2 flow. After nearly two hours of adsorption, the samples with 15, 20, and 30 wt.% PEI exhibited adsorption curves that approached equilibrium, while those with 45 and 50 wt.% PEI continued to show increasing mass, indicating that equilibrium had not yet been reached. As expected, the cumulative CO_2 uptake increased with increasing PEI loading, owing to the greater availability of amine active sites.

A comparison of the 15, 20, and 30 wt.% PEI samples further highlights that higher PEI loadings led to steeper initial slopes in the uptake curves and an earlier transition into the slower, quasi-equilibrium phase. This indicates faster initial adsorption rates, which can be attributed to the abundance of available amine sites at the beginning of the process. Notably, no pore blockage was observed in these samples (panels (a), (b), and (c) in Figure A.2), which ensured efficient access of CO_2 molecules to internal reaction sites. In contrast, comparing the samples with 30, 45, and 50 wt.% PEI loadings revealed an opposite trend in the initial adsorption rates. The 30 wt.% sample exhibited the fastest initial uptake among the three. At higher PEI contents ($\geq$ 45 wt.%), a surface layer of PEI was observed to form, as seen in panel (d) of Figure A.2. This thick polymer layer increased the diffusion path length and resistance for CO_2 transport, while also reducing the effective surface area for gas–solid interactions. Consequently, the contact probability between CO_2 and amine sites decreased, and the buried reactive sites became less accessible during the early stages of adsorption. However, as the process continued, CO_2 molecules gradually diffused deeper into the PEI layer and reacted with previously unoccupied internal amine sites. Despite the hindered diffusion, the total uptake for high-loading samples continued to rise over time, highlighting the latent capacity stored in the inner regions of the thick PEI layer.

Here, the adsorption curves have been roughly divided into two stages: a rapid uptake phase followed by a slower, diffusion-controlled phase. However, this division remains qualitative. A more detailed interpretation of these stages will be presented in the following section through kinetic model fitting.

3.3 Influence of Porous Titania Support Structures on CO_2 Adsorption

To evaluate the influence of structural asymmetry on CO_2 adsorption behavior, amine-impregnated asymmetric TiO_2 supports were systematically compared with TiO_2 supports with alternating gyroid (TiO_2-G^A) architecture under various operational conditions. Panels (a) and (b) in Figure 3.3 present the CO_2 adsorption profiles of samples with varying PEI loadings (20, 30, 50 wt.%) under a pure CO_2 flow of 60 mL/min at 100 °C where in panel (b) the data from (a) is normalized to surface area. Both asymmetric and gyroidal samples were included to enable direct comparison. Panels (c) and (d) in Figure 3.3 further examines the effects of gas flow rate on CO_2 uptake capacity for 20 wt.% PEI-impregnated samples of each morphology, tested at 100 °C in pure CO_2.

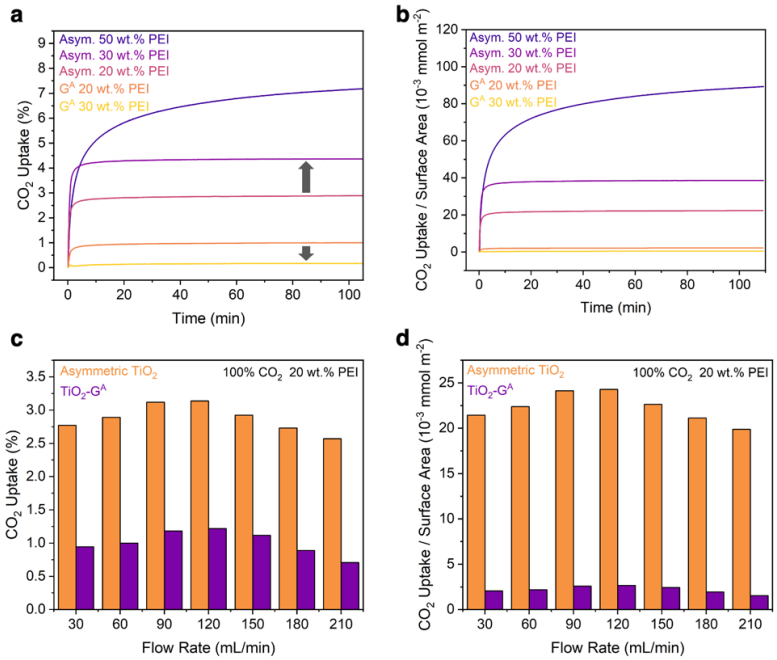

Figure 3.3. Comparison of CO_2 adsorption behavior between PEI-impregnated asymmetric TiO_2 and TiO_2-G^A. (a, b) CO_2 uptake profiles of TiO_2 samples with different PEI loadings (20–50 wt.%) measured under 100 °C and pure CO_2 flow at 60 mL/min, shown as (a) uptake percentage and (b) uptake normalized by surface area of the support. (c, d) Effects of CO_2 flow rate (30–210 mL/min) on CO_2 adsorption by 20 wt.% PEI-impregnated asymmetric TiO_2 and TiO_2-G^A at 100 °C, shown as (c) uptake percentage and (d) uptake normalized by surface area of the support.

3.3.1 Structure-Driven Enhancement in CO_2 Uptake

From panel (a) in Figure 3.3, TiO_2 samples with asymmetric pore morphology exhibited significantly higher CO_2 uptake than TiO_2-G^A samples at the same PEI loading. For instance, at 20 wt.% PEI loading, the asymmetric TiO_2 sample achieved a CO_2 uptake of 2.9%, nearly three times that of the G^A sample (1.0%). At 30 wt.% loading, this difference became even more pronounced: the asymmetric sample reached 4.3%, while the G^A sample showed only 0.17% uptake, indicating a 25-fold increase. This striking disparity arises primarily from differences in pore structure and PEI distribution. Compared to the asymmetric architecture, the G^A structure inherently featured smaller pore sizes and a denser, less accessible pore network, which limits gas transport. Upon PEI impregnation, both samples experienced reductions in interconnected porosity and pore diameter; however, the impact was far more severe for the G^A sample. Notably, the 30 wt.% PEI-impregnated G^A sample presented here was prepared without vacuum pre-treatment, similar to the corresponding asymmetric TiO_2 sample. As a result, a dense layer of PEI accumulated on the external surface, severely blocking open pores and preventing efficient gas diffusion into the internal structure.

Consistent with the trends discussed in the previous section, increasing PEI loading enhanced CO_2 uptake for asymmetric TiO_2, owing to the increased availability of amine sites. In stark contrast, for the G^A samples, increasing the PEI loading from 20 to 30 wt.% led to a reduction in CO_2 uptake. This clearly highlights the beneficial effects of the non-equilibrium derived asymmetric TiO_2 support structure relative to the equilibrium G^A network structure. CO_2 adsorption data for 50 wt.% PEI-loaded G^A samples are not presented here, as the G^A structure could not accommodate such high

PEI loadings without entirely blocking the pores, regardless of whether vacuum pre-treatment was applied.

To decouple the effects of surface area, in panel (b) of Figure 3.3 the adsorption data of panel (a) were normalized by the BET surface area of the corresponding TiO_2 supports. Because G^A exhibited a higher surface area than the asymmetric structure (130 vs. 36.7 m^2/g, see Table 3.1), normalization therefore revealed an even more striking contrast. At 20 wt.% PEI loading, the normalized uptake of asymmetric TiO_2 was over nine times that of G^A, *i.e.*, almost an order of magnitude, while at 30 wt.%, it is nearly 100 times greater, *i.e.*, almost two orders of magnitude. These findings clearly reveal that total surface area is not the dominant factor governing adsorption performance. The superior CO_2 uptake of asymmetric TiO_2 is attributed to a superior balance between mass transport and surface area within the materials enhancing gas diffusion efficiency *and* internal PEI accessibility, all enabled by its asymmetric pore morphology with large finger-like macropores and mesoporous walls.

3.3.2 Sustained Adsorption Performance under High Flow Rates

The effects of CO_2 flow rate on the adsorption performance of PEI-impregnated asymmetric TiO_2 and TiO_2-G^A samples is shown in panel (c) of Figure 3.3, with the associated surface area-normalized uptake displayed in panel (d). Both asymmetric TiO_2 the TiO_2-G^A samples exhibited their highest uptake at moderate flow rates of 90 and 120 mL/min. This observation aligns with the general understanding that while increasing gas flow enhances external convection, CO_2 transport within porous adsorbents is predominantly governed by diffusion. As such, variations in flow rate have

limited influence on the overall diffusion process inside the material. At their respective optimal flow conditions, the G^A samples achieved less than 40% of the CO_2 uptake attained by the asymmetric TiO_2, and across all tested flow rates, the asymmetric samples consistently outperformed G^A by a factor of 2.5 to 3. After normalizing the data by BET surface area to account for differences in total surface area between the two TiO_2 supports, the performance gap became even more pronounced, again highlighting the critical role of amine-accessible porosity and internal connectivity in governing adsorption efficiency.

Notably, very high flow rates such as 180 and 210 mL/min have rarely been explored in previous CO_2 capture studies, which often operate below 100 mL/min. Interestingly, the asymmetric TiO_2 still maintained robust performance under flow rates of 180 and 210 mL/min, achieving 87% and 82% of the maximum uptake observed at the optimal flow rate, respectively. Under the same conditions, the TiO_2-G^A samples achieved only 72% and 57% of their respective maxima. This suggests that the asymmetric structure supports rapid gas diffusion and efficient utilization of amine sites even under high-throughput conditions, offering potential advantages for practical applications requiring fast cycling or high gas throughput.

3.4 Adsorption Kinetics Studies

As mentioned at the end of section 3.2, the CO_2 adsorption could be broadly divided into two stages: an initial rapid uptake followed by a slower increase. However, further kinetic analyses revealed that the overall adsorption process consisted of three distinct stages.

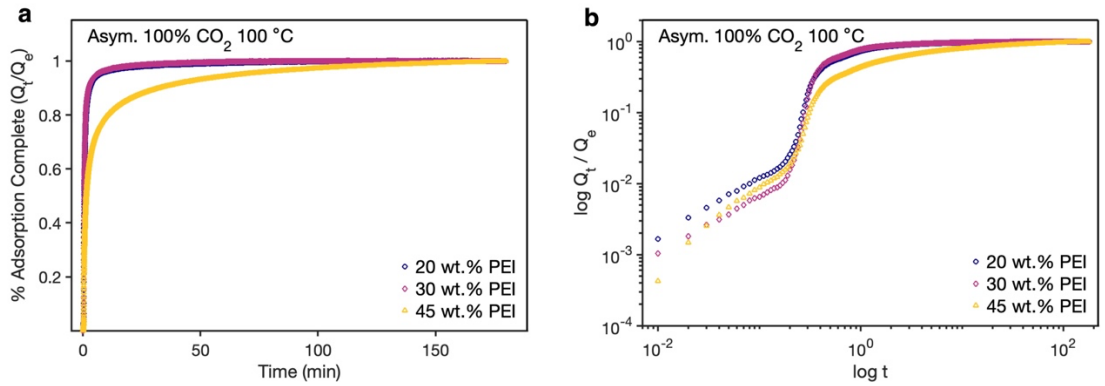

Figure 3.4. Pure CO_2 adsorption profiles of PEI-impregnated asymmetric TiO_2 at 100 °C in a 60 mL/min flow: (a) % Adsorption Complete (Q_t/Q_e) vs. time (t), and (b) log Q_t/Q_e vs. log t.

In panel (a) of Figure 3.4, the y-axis represents the fractional adsorption completed over time, defined as Q_t/Q_e, where Q_t is the amount of CO_2 adsorbed at time t, and Q_e is the equilibrium adsorption capacity. This representation highlights the adsorption kinetics as a function of time for samples with different PEI loadings: 20 wt.% (blue circles), 30 wt.% (pink diamonds), and 45 wt.% (yellow triangles). The curves for the 20 and 30 wt.% samples appeared nearly indistinguishable. Meanwhile, the 45 wt.% PEI sample displayed a slower adsorption rate and delayed progression toward equilibrium, as reflected in the gentler slope and extended time required to reach saturation. This behavior is consistent with the trend described earlier (see section 3.2) regarding the influence of PEI loading on CO_2 uptake.

Panel (b) in Figure 3.4 presents the same datasets as in panel (a) but plotted in log(Q_t/Q_e) versus log(t) form. This log–log representation serves to magnify the early-stage kinetics and distinguish between different kinetic regimes, something that linear–linear plots often obscure, especially in the initial seconds of fast adsorption processes. From differences in slopes in this plot, we can clearly identify three distinct stages of the CO_2 adsorption process:

1. Stage I: From ~0.01 to ~0.2 min, the data points formed an approximately straight line, suggesting one kinetic mechanism dominating this early stage.
2. Stage II: Between ~0.2 and ~0.8 min, the curves displayed another regime with a much steeper rise.
3. Stage III: After ~0.8 min began a third regime in which the curves started to level off, suggesting a transition into a slower phase of adsorption as the system gradually progressed toward equilibrium.

Given the presence of these three kinetically distinct regimes, the log–log adsorption curves were subsequently fitted using a composite kinetic model designed to capture the dynamics of each stage. The overall function of the kinetic model is presented in Equations (1-4).

$$f(t) = a_1 f_1(\min(t, t_1)) + a_2 \cdot f_2(\max(0, t - t_1)) + a_3 \cdot f_3(\max(0, t - t_1)) \quad (1)$$

$$f_1(t) = A \cdot t^b \quad (2)$$

$$f_2(t) = 1 - e^{-\left(\frac{t}{\tau_2}\right)^n} \quad (3)$$

$$f_3(t) = \frac{t}{t + \frac{\tau_3}{Q_e}} \quad (4)$$

The pre-factors a_1, a_2 and a_3 in the overall function satisfy the constraint $a_1 + a_2 + a_3 = 1$ Therefore, the equation can also be rewritten as:

$$f(t) = \begin{cases} a_1 \cdot A \cdot t^b, & if\ t < t_1 \\ a_1 \cdot A \cdot {t_1}^b + a_2 \cdot \left[1 - e^{-(\frac{t-t_1}{\tau_2})^n}\right] + a_3 \cdot \dfrac{t - t_1}{t - t_1 + \frac{\tau_3}{Q_e}}, & if\ t \geq t_1 \end{cases} \quad (5)$$

The adsorption profiles were fitted with the composite kinetic model of Eqn. (5). Representative fitting results are presented in Figure 3.5. As is evident from this

representation, the model yields excellent fits for both PEI-impregnated asymmetric TiO_2 (panels a & c) and TiO_2-G^A (panels b & d) samples under high-temperature (100 °C, panels a & b) and ambient-temperature (40 °C, panels c & d) conditions, confirming its capability to effectively capture the dynamics of each adsorption stage across all stages over the entire time scale tested.

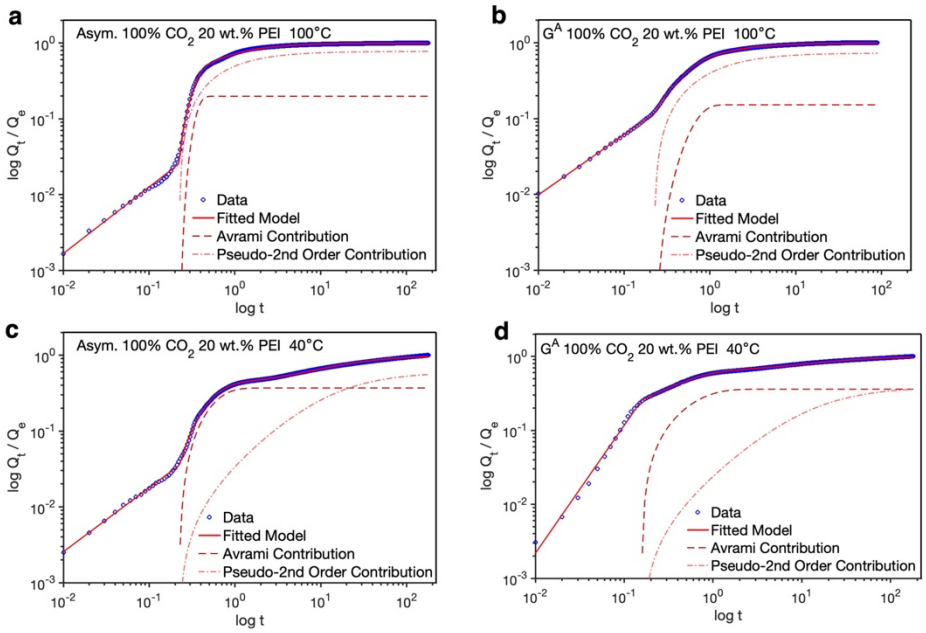

Figure 3.5. Log-log representation and fitting for the adsorption of pure (100%) CO_2 at 100 °C (a, b) and 40 °C (c, d) on 20 wt.% PEI-impregnated asymmetric TiO_2 (a, c), and TiO_2-G^A (b, d). Open symbols: experimental data; solid lines: fitted model. In addition to data and fits, specific fit components as shown separately in each panel: dashed lines: Avrami model contribution; and dash-dot lines: pseudo-second order model contribution.

The first stage extends from the start of CO_2 flow to a characteristic time point t_1. As shown by the approximately linear trend in the log–log plots, this earliest phase is governed by a single kinetic mechanism. Accordingly, the adsorption behavior can be effectively captured by the power-law expression in Eqn. (2), which is often used to describe the adsorption on heterogeneous surfaces[37]. The contribution of this stage to the overall adsorption process becomes essentially fixed after t_1, represented by the pre-factor a_1. Given the short duration and rapid rise in CO_2 uptake, this stage is attributed

primarily to physisorption. During this stage, CO_2 molecules displace the N_2 purge gas in the system and interact with the surface of the PEI layer, leading to fast, reversible adsorption. While physisorption reaches equilibrium rapidly, this does not imply the process has ceased; rather, a dynamic balance between adsorption and desorption is established, resulting in no net change in the apparent uptake beyond this stage.

Following this initial stage I, adsorption enters a steeper, nonlinear region beginning at t_1. This stage II is described by the Avrami model in Eqn. (3), where the Avrami exponent, n, defines the steepness of the uptake curve and the characteristic time constant, τ_2, reflects the kinetic timescale of this stage. Originally developed to describe nucleation-and-growth kinetics[38], the Avrami model has recently been adopted to characterize chemisorption in amine-functionalized mesoporous silica materials[39]. Mechanistically, during this stage, CO_2 molecules diffuse into the amine-impregnated film and interact with reactive amine groups located on the outer surface of the PEI layer. While physisorption continues to a minor extent, chemisorption, which is typically a slower but stronger binding process, becomes the dominant mechanism. Therefore, stage II can be regarded as a reaction-controlled chemisorption process.

The transition from stage II to stage III was not well defined across all samples. In panels (a), (c), and (d) of Figure 3.5, stage II ended with a plateau before a new increase in uptake signaled the onset of stage III. In contrast, panel (b) of Figures 3.5 showed no clear boundary between these two stages, suggesting a more gradual transition. Nevertheless, stage III is consistently characterized by a pronounced slowdown in the adsorption rate, with the curves gradually approaching a plateau as time progresses. This final stage is described by the pseudo-second order kinetic model

in Eqn. (4), which is frequently used to represent chemisorption processes involving covalent or ionic bonding[40]. Here, the characteristic time constant, τ_3, captures the timescale of this slow adsorption process and the pre-factor, a_3, its amplitude. At this stage, CO_2 continues to diffuse inward from the outer surface, reaching amine sites buried deep within the PEI layer. The adsorption kinetics here are no longer limited by surface availability but are instead governed by the internal diffusion and accessibility of reactive sites. As such, the entire stage is a diffusion-controlled chemisorption process.

In summary, rather than proceeding through a single separated stage, the CO_2 adsorption process beyond t_1 involves two separate kinetic mechanisms. To quantitatively account for this interplay, the CO_2 uptake beyond t_1 was modeled as a weighted combination of Avrami and pseudo-second order expressions**,** with their respective contributions captured by the pre-factors a_2 and a_3 in Eqn. (5).

To further investigate details of the three-stage characteristics of each adsorption process, multiple datasets were fitted using Eqn. (5). The resulting fits and comparisons are discussed in the following subsections.

3.4.1 Adsorption Kinetics at Different Adsorption Temperatures: Asymmetric TiO_2 vs. TiO_2-G^A Samples

As pointed out earlier, log-log fittings for the adsorption of pure CO_2 at 100 °C and 40 °C on 20 wt.% PEI-impregnated asymmetric TiO_2 compared to TiO_2-G^A film samples is shown in Figure 3.5, while the corresponding fitting parameters are summarized in Table 3.2. The degree of kinetic separation between the Avrami and

pseudo-second-order processes was influenced by both the support structure and the adsorption temperature. For the asymmetric TiO_2 sample (panels a & c in Figure 3.5), the two processes were clearly temporally separated, with stage II ending in a brief plateau before stage III begins. This separation became even more pronounced at lower temperature (40 °C), as reflected in the large difference between the time scale of the absorption process of stage II (τ_2 = 0.570 min) versus that of stage III (τ_3 = 27.6 min). The pre-factor, a_3, decreased from 77.6% to 59.6%, suggesting that although deep chemisorption remains the dominant mechanism, its contribution is reduced at lower temperature. This is likely due to the hindered diffusion of CO_2 within the PEI matrix at lower temperature, which limits the extent of internal chemisorption and thus lowers its contribution to the overall uptake.

In contrast, for the TiO_2-G^A sample, the separation between the two kinetic stages was less distinct, particularly at 100 °C (panel b in Figure 3.5), where the contributions from the Avrami and pseudo-second-order models rose nearly concurrently (τ_2 = 0.705 min, τ_3 = 1.06 min), indicating a substantial overlap in the associated adsorption processes. At 40 °C (panel d in Figure 3.5), a strong degree of separation became apparent (τ_2 = 0.577 min versus τ_3 = 23.2 min), though it remained less pronounced than in the asymmetric sample at the same temperature. These observations suggest that although temperature affects the degree of separation between the different kinetic phases, the morphology of the TiO_2 support plays a more decisive role. The asymmetric structure, with its directional and hierarchical porosity, enables staged gas transport and enhances diffusion-controlled chemisorption. This structural advantage promotes more effective amine utilization and sustained CO_2 uptake.

Table 3.2. Parameters from log-log Fittings for the Adsorption of Pure CO_2 at 100 °C and 40 °C on 20 wt.% PEI-Impregnated Asymmetric TiO_2 and TiO_2-G^A Film Samples.

Temperature (°C)	Sample	Stage I		Stage II			Stage III		R^2
		a_1	t_1 (min)	a_2	n	τ_2 (min)	a_3	τ_3 (min)	
100 °C	Asymmetric TiO_2	2.56%	0.225	19.9%	2.46	0.366	77.6%	1.36	0.9989
	TiO_2-G^A	11.7%	0.224	15.2%	1.95	0.705	73.1%	1.06	0.9992
40 °C	Asymmetric TiO_2	3.50%	0.222	36.9%	1.27	0.570	59.6%	27.6	0.9913
	TiO_2-G^A	25.6%	0.157	36.0%	1.00	0.577	38.4%	23.2	0.9967

It is noteworthy that for the G^A sample at both temperatures, the y-axis value at the transition point between stages I and II was higher than that of the asymmetric sample, indicating a larger relative contribution from stage I to the overall CO_2 uptake. For example, the pre-factor, a_1, corresponding to stage I, reached 11.7% at 100 °C and 25.6% at 40 °C for the TiO_2-G^A sample, compared to only 2.6% and 3.5% for the asymmetric sample, respectively. Inversely, this suggests that chemisorption plays less of a relative role in the overall CO_2 uptake of the TiO_2-G^A sample than it does for the asymmetric sample. Since the capacity of physisorption is inherently limited relative to chemisorption, this is consistent with the lower overall CO_2 uptake observed for the TiO_2-G^A sample compared to the asymmetric structure.

3.4.2 Adsorption Kinetics at Different CO_2 Concentration: 20 wt.% PEI-Impregnated Asymmetric TiO_2 vs. TiO_2-G^A

In Figure A.9 and summarized in Table A.1, fits of the adsorption kinetics of 20 wt.% PEI-impregnated asymmetric TiO_2 and TiO_2-G^A samples under CO_2 concentrations of 100%, 15% and 5% are presented. Consistent with observations in section 3.4.1, the kinetic separation between stages II and III remained relatively distinct in the asymmetric sample compared with in the gyroidal sample across all

concentrations. Notably, in the TiO_2-G^A samples under 15% and 5% CO_2, the time scales for the process fitted with a pseudo-second order expression (formerly referred to as stage III) as expressed by the time constant, τ_3, was shorter than those for the process fitted with the Avrami expression (formerly stage II) as expressed by the time constant, τ_2, e.g., τ_3 = 1.29 min vs. τ_2 = 1.37 min at 15% CO_2. This implies that the slower deep chemisorption process (stage III) completes before the stage II is finished, which is counterintuitive from a typical kinetic progression perspective. This phenomenon likely arises from the constrained internal diffusion environment in the PEI-impregnated gyroidal network. Although the surface pores may remain accessible, the inner channels of the G^A are prone to being partially blocked or narrowed after PEI impregnation. As a result, the driving force for CO_2 penetration into deeper regions is significantly reduced, especially under low CO_2 concentration, where the chemical potential gradient is weaker. In contrast, the asymmetric TiO_2 structure features a more hierarchical, open morphology, with PEI distributed more uniformly across accessible surfaces. This allows also sequential CO_2 transport and reaction within the inner PEI layers, extending the duration of Stage III even at low CO_2 concentrations.

For both materials, the duration of stage I (t_1) increased slightly as CO_2 concentration decreased, while its relative contribution (a_1) became smaller. This is expected because lower CO_2 concentrations result in reduced adsorption driving force, slower initial uptake, and lower equilibrium capacity. As a result, the initial physisorption stage took longer to reach dynamic equilibrium but ultimately contributed less to the total CO_2 capture.

There was a notable shift observed in the distribution of adsorption between stages II and III as CO_2 concentration decreases. The relative heights of the dashed (Avrami) and dash-dot (pseudo-second order) lines in the log–log plots in Figure A.9 provide a visual indication of their respective contributions. When the pseudo-second-order curve lay above the Avrami one (panel a in Figure A.9), it signified a dominant stage III contribution. Under 100% CO_2, the dominant contribution to overall uptake lay in stage III, with a_3 values of 77.6% (asymmetric) and 73.1% (G^A). However, at 15% and 5%, the balance tilted toward stage II, with a_2 exceeding 80% for asymmetric TiO_2 and ~60% for G^A. This reflected the reduced extent of internal diffusion-controlled chemisorption under diluted CO_2 atmospheres, leaving the reaction-driven chemisorption as the dominant mechanism. These observations reinforce the idea that CO_2 concentration influences not only the overall capacity and rate, but also the relative contribution of different kinetic stages, depending on the specific material morphology.

3.4.3 Adsorption Kinetics in Asymmetric TiO_2: Effect of PEI Loading

So far, the CO_2 adsorption kinetics was discussed only for samples with 20 wt.% PEI loading. To better understand how varying PEI loadings for asymmetric TiO_2 samples affect the adsorption kinetics, Figure A.10 and Table A.2 present the log–log fitting curves and extracted parameters, for asymmetric TiO_2 samples with 20, 30, and 45 wt.% PEI loadings under CO_2 concentrations of 100%, 15%, and 5%, respectively. Across all CO_2 concentrations, the adsorption behavior was dependent of PEI loading. At 20 and 30 wt.% PEI, the uptake was dominated by diffusion-controlled chemisorption, especially under 100% CO_2, where stage III contributed over 70% of the

total adsorption (e.g., 77.6% at 20 wt.% and 71.0% at 30 wt.%). In contrast, at 45 wt.% PEI, the contributions from stages II and III became more balanced, with a_2 and a_3 values converging (46.4% vs. 51.2% under 100% CO_2). This shift indicated that increasing PEI content led to more evenly distributed contributions of the two chemisorption processes, though they remained kinetically separated in timescale (compare values of τ_2 and τ_3 in Table A.2).

Further supporting this observation, the time constants τ_3 for stage III increase substantially with PEI loading. At 100% CO_2, τ_3 rose from 1.36 min at 20 wt.% PEI to 39.7 min at 45 wt.% PEI, suggesting that the diffusion-limited process becomes increasingly delayed as the PEI accumulates within the pore structure. At lower CO_2 concentrations (15% and 5%), a similar trend emerged, particularly at 30 and 45 wt.% PEI where τ_3 greatly exceeded τ_2 (see Table A.2), implying that diffusion-controlled chemisorption continues long after the reaction-controlled CO_2 uptake has plateaued. These findings suggest that higher PEI loadings introduce more complex diffusion environments within the asymmetric structure, possibly due to increased PEI layer thickness and possible pore clogging.

CHAPTER 4

CONCLUSION AND OUTLOOK

Amine-functionalized porous solid sorbents are among the most effective materials for post-combustion CO_2 capture, with amine-loaded MCM-41 widely used due to its tunable mesopores and high surface area. However, its poor hydrothermal stability hinders long-term industrial use especially for CO_2 capture at higher temperatures. To address this challenge, we developed robust yet tunable adsorbent supports from block copolymer self-assembly directed titania with thick and stable walls. Particular emphasis of this study was on elucidating possible advantages from working with non-equilibrium based asymmetric porous TiO_2 films prepared via the scalable SNIPS process. Their CO_2 capture characteristics were compared to those of equilibrium derived mesoporous alternating gyroidal (G^A) TiO_2 controls (TiO_2-G^A), the most open and continuous mesostructure obtained from block copolymer self-assembly. When both porous supports were surface coated with amine-group containing polymer PEI, the asymmetric films offered superior processability, requiring neither vacuum pre-treatment nor excessive PEI concentrations to achieve equivalent PEI loading levels. Structural characterization confirmed the distinct pore geometry of these two support structures. TGA-based CO_2 adsorption measurements revealed that, across all tested conditions, including varying temperature, flow rate, CO_2 concentration, and PEI loading, the asymmetric TiO_2 consistently outperformed the G^A control, often achieving

2.5–3 times higher uptake per sample weight or almost an order of magnitude when results were normalized to surface area.

A composite kinetic model was developed to interpret the observed multistage adsorption behavior, identifying three sequential stages: physisorption described by a power-law expression, reaction-controlled chemisorption described by the Avrami model, and diffusion-controlled chemisorption characterized by a pseudo-second-order model. Much clearer separation between these three stages for CO_2 adsorption on the asymmetric samples underscored the synergistic role of pore morphology and PEI accessibility in enhancing adsorbent performance. Combined with the inherent scalability of SNIPS-derived membranes and the thermal and hydrothermal resilience of the TiO_2 framework, this work positions asymmetric TiO_2 films as a promising platform for next-generation CO_2 capture. Beyond carbon capture, the design principles demonstrated here—fast mass transport and high accessible surface area enabled by structural asymmetry—may be broadly applicable to other gas separation technologies.

Despite the excellent thermal and hydrothermal stability of TiO_2, its relatively high density remains a limitation when adsorbent performance is evaluated on a per-mass basis, which is a standard metric in CO_2 capture. Furthermore, since TiO_2 under illumination by sunlight is known to exhibit self-cleaning properties, a non-reactive material like amorphous silica, which also has much lower density than TiO_2, may be advantages as asymmetric support. Future efforts should thus focus on developing asymmetric, hierarchically porous adsorbents based on lower-density materials, such as silica and alumina, to further improve the gravimetric performance of amine-functionalized adsorbents. By integrating the structural advantages of asymmetry and

hierarchical porosity with lightweight and unreactive frameworks, the next-generation solid adsorbents may achieve even higher efficiency and broader applicability for industrial scale CO_2 sequestration.

REFERENCE

1. Sreedhar, I., Nahar, T., Venugopal, A. & Srinivas, B. Carbon capture by absorption – Path covered and ahead. *Renew. Sustain. Energy Rev.* **76**, 1080–1107 (2017).

2. Thi Le, M. U., Lee, S.-Y. & Park, S.-J. Preparation and characterization of PEI-loaded MCM-41 for CO2 capture. *Int. J. Hydrog. Energy* **39**, 12340–12346 (2014).

3. Hack, J., Maeda, N. & Meier, D. M. Review on CO2 Capture Using Amine-Functionalized Materials. *ACS Omega* **7**, 39520–39530 (2022).

4. Martell, J. D., Milner, P. J., Siegelman, R. L. & Long, J. R. Kinetics of cooperative CO $_2$ adsorption in diamine-appended variants of the metal–organic framework Mg $_2$ (dobpdc). *Chem. Sci.* **11**, 6457–6471 (2020).

5. Dziejarski, B., Serafin, J., Andersson, K. & Krzyżyńska, R. CO2 capture materials: a review of current trends and future challenges. *Mater. Today Sustain.* **24**, 100483 (2023).

6. Bhown, A. S. & Freeman, B. C. Analysis and status of post-combustion carbon dioxide capture technologies. *Environ. Sci. Technol.* **45**, 8624–8632 (2011).

7. Ramezan, M. *et al. Carbon Dioxide Capture from Existing Coal-Fired Power Plants*. 229 (2007).

8. *Porous Materials for Carbon Dioxide Capture*. (Springer, Berlin, Heidelberg, 2014). doi:10.1007/978-3-642-54646-4.

9. Mason, J. A. *et al.* Application of a high-throughput analyzer in evaluating solid adsorbents for post-combustion carbon capture via multicomponent adsorption of CO2, N2, and H2O. *J. Am. Chem. Soc.* **137**, 4787–4803 (2015).

10. Chaikittisilp, W., Didas, S. A., Kim, H.-J. & Jones, C. W. Vapor-Phase Transport as A Novel Route to Hyperbranched Polyamine-Oxide Hybrid Materials. *Chem. Mater.* **25**, 613–622 (2013).

11. Cai, H. *et al.* Preparation and characterization of novel carbon dioxide adsorbents based on polyethylenimine-modified Halloysite nanotubes. *Environ. Technol.* **36**, 1273–1280 (2015).

12. Varghese, A. M. & Karanikolos, G. N. CO2 capture adsorbents functionalized by amine – bearing polymers: A review. *Int. J. Greenh. Gas Control* **96**, 103005 (2020).

13. Zhao, D. *et al.* Triblock Copolymer Syntheses of Mesoporous Silica with Periodic 50 to 300 Angstrom Pores. *Science* **279**, 548–552 (1998).

14. Bates, F. S. & Fredrickson, G. H. Block Copolymer Thermodynamics: Theory and Experiment. *Annu. Rev. Phys. Chem.* **41**, 525–557 (1990).

15. Warren, S. C. *et al.* Ordered mesoporous materials from metal nanoparticle-block copolymer self-assembly. *Science* **320**, 1748–1752 (2008).

16. Beaucage, P. A., Van Dover, R. B., DiSalvo, F. J., Gruner, S. M. & Wiesner, U. Superconducting Quantum Metamaterials from Convergence of Soft and Hard Condensed Matter Science. *Adv. Mater.* **33**, 2006975 (2021).

17. Hesse, S. A. Asymmetric Porous Materials from Non-Equilibrium Block Copolymer Self-Assembly for Separation, Catalysis, and Energy Storage Applications. (Cornell University, 2019).

18. Hesse, S. A. *et al.* Materials Combining Asymmetric Pore Structures with Well-Defined Mesoporosity for Energy Storage and Conversion. *ACS Nano* **14**, 16897–16906 (2020).

19. Peinemann, K.-V., Abetz, V. & Simon, P. F. W. Asymmetric superstructure formed in a block copolymer via phase separation. *Nat. Mater.* **6**, 992–996 (2007).

20. Tsaur, L. & Wiesner, U. B. Non-Equilibrium Block Copolymer Self-Assembly Based Porous Membrane Formation Processes Employing Multicomponent Systems. *Polymers* **15**, 2020 (2023).

21. Moore, W. *et al.* Asymmetric Porous Catalyst Structures for Low-Temperature Photocatalytic Dry Reforming of Methane. *ACS Nano* acsnano.5c04286 (2025) doi:10.1021/acsnano.5c04286.

22. Phillip, W. A. *et al.* Tuning Structure and Properties of Graded Triblock Terpolymer-Based Mesoporous and Hybrid Films. *Nano Lett.* **11**, 2892–2900 (2011).

23. Robbins, S. W., Sai, H., DiSalvo, F. J., Gruner, S. M. & Wiesner, U. Monolithic gyroidal mesoporous mixed titanium-niobium nitrides. *ACS Nano* **8**, 8217–8223 (2014).

24. Brunauer, S., Emmett, P. H. & Teller, E. Adsorption of Gases in Multimolecular Layers. *J. Am. Chem. Soc.* **60**, 309–319 (1938).

25. Sing, K. S. W. Reporting physisorption data for gas/solid systems with special reference to the determination of surface area and porosity (Recommendations 1984). *Pure Appl. Chem.* **57**, 603–619 (1985).

26. Barrett, E. P., Joyner, L. G. & Halenda, P. P. The Determination of Pore Volume and Area Distributions in Porous Substances. I. Computations from Nitrogen Isotherms. *J. Am. Chem. Soc.* **73**, 373–380 (1951).

27. Xu, X., Song, C., Andrésen, J. M., Miller, B. G. & Scaroni, A. W. Preparation and characterization of novel CO2 "molecular basket" adsorbents based on polymer-modified mesoporous molecular sieve MCM-41. *Microporous Mesoporous Mater.* **62**, 29–45 (2003).

28. Werber, J. R., Osuji, C. O. & Elimelech, M. Materials for next-generation desalination and water purification membranes. *Nat. Rev. Mater.* **1**, 16018 (2016).

29. Guldin, S. *et al.* Self-Cleaning Antireflective Optical Coatings. *Nano Lett.* **13**, 5329–5335 (2013).

30. Lang, C., Kumar, M. & Hickey, R. J. Current status and future directions of self-assembled block copolymer membranes for molecular separations. *Soft Matter* **17**, 10405–10415 (2021).

31. Lahn, L., Bertier, P., Seemann, T. & Stanjek, H. Distribution of sorbed water in the pore network of mudstones assessed from physisorption measurements. *Microporous Mesoporous Mater.* **295**, 109902 (2020).

32. Calvert, J. G. Glossary of atmospheric chemistry terms (Recommendations 1990). *Pure Appl. Chem.* **62**, 2167–2219 (1990).

33. Miao, Y., He, Z., Zhu, X., Izikowitz, D. & Li, J. Operating temperatures affect direct air capture of CO2 in polyamine-loaded mesoporous silica. *Chem. Eng. J.* **426**, 131875 (2021).

34. Ahmed, S., Ramli, A. & Yusup, S. Development of polyethylenimine-functionalized mesoporous Si-MCM-41 for CO2 adsorption. *Fuel Process. Technol.* **167**, 622–630 (2017).

35. Yu, K. *et al.* Sol–gel synthesis and hydrothermal processing of anatase nanocrystals from titanium *n*-butoxide. *Mater. Lett.* **59**, 2515–2518 (2005).

36. Tsioptsias, C. On the latent limit of detection of thermogravimetric analysis. *Measurement* **204**, 112136 (2022).

37. Valtcheva, E. T. Power rate law in kinetics of adsorption processes on exponentially inhomogeneous surfaces. *React. Kinet. Catal. Lett.* **29**, 137–144 (1985).

38. Avrami, M. Kinetics of Phase Change. I General Theory. *J. Chem. Phys.* **7**, 1103–1112 (1939).

39. Monazam, E. R. *et al.* Equilibrium and kinetics analysis of carbon dioxide capture using immobilized amine on a mesoporous silica. *AIChE J.* **59**, 923–935 (2013).

40. Ho, Y. S. & McKay, G. Pseudo-second order model for sorption processes. *Process Biochem.* **34**, 451–465 (1999).

APPENDIX

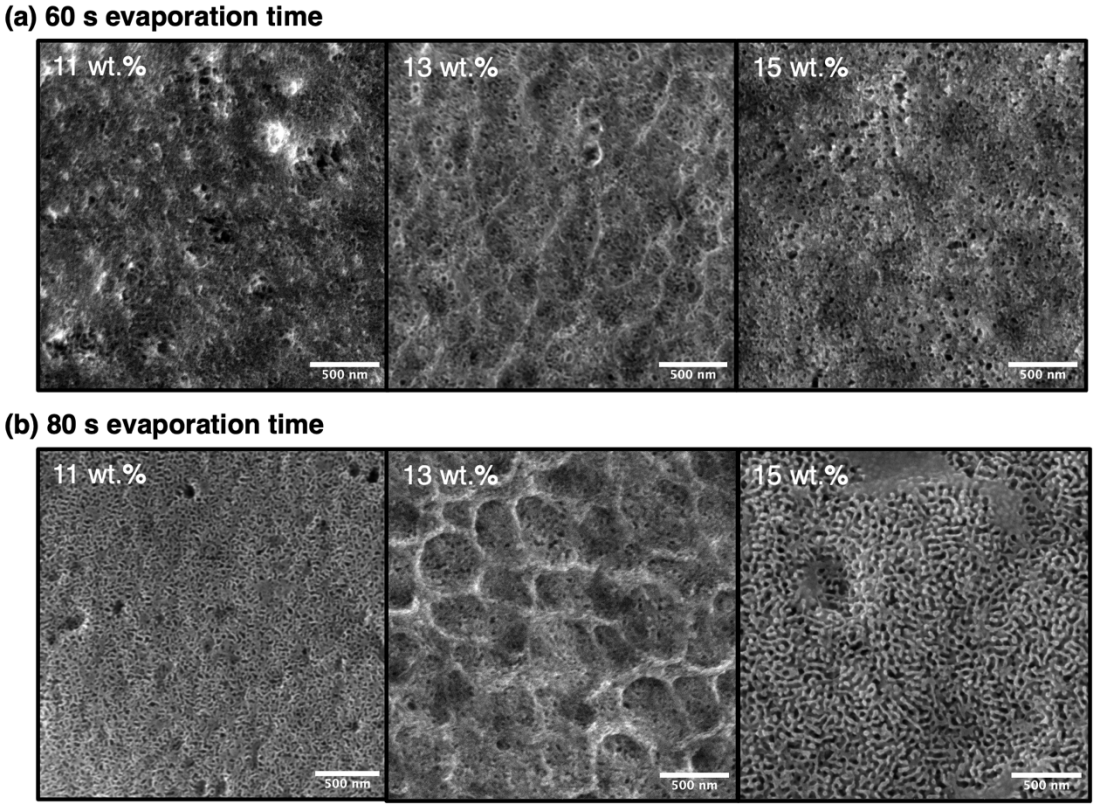

Figure A.1. Top surface SEM images of asymmetric TiO_2 prepared with different evaporation times in the SNIPS process: (a) 60 s versus (b) 80 s. From left to right, polymer concentrations of dope solution ranged from 11 wt.% and 13 wt.% all the way to 15 wt.%, as indicated.

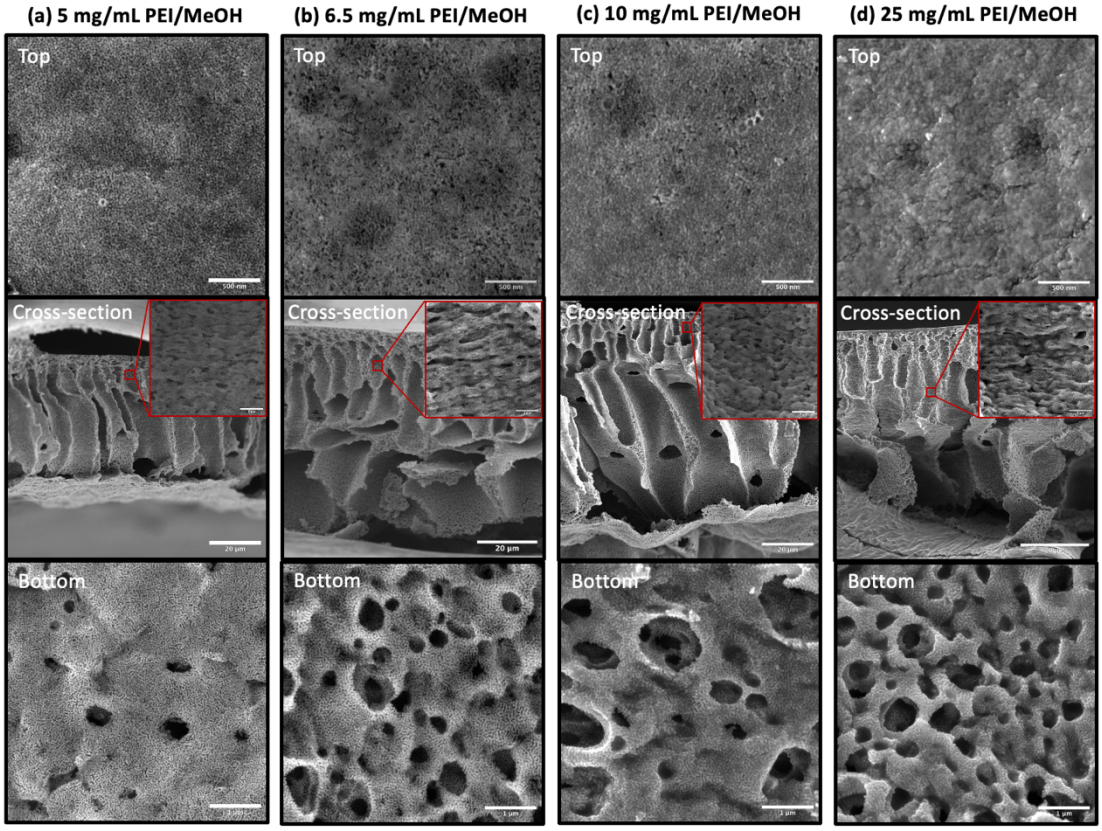

Figure A.2. SEM images of amine-impregnated asymmetric TiO_2 prepared using PEI/MeOH solutions of increasing concentrations: (a) 5 mg/mL, (b) 6.5 mg/mL, (c) 10 mg/mL, and (d) 25 mg/mL. From top to bottom: top surface, cross-section, and bottom surface.

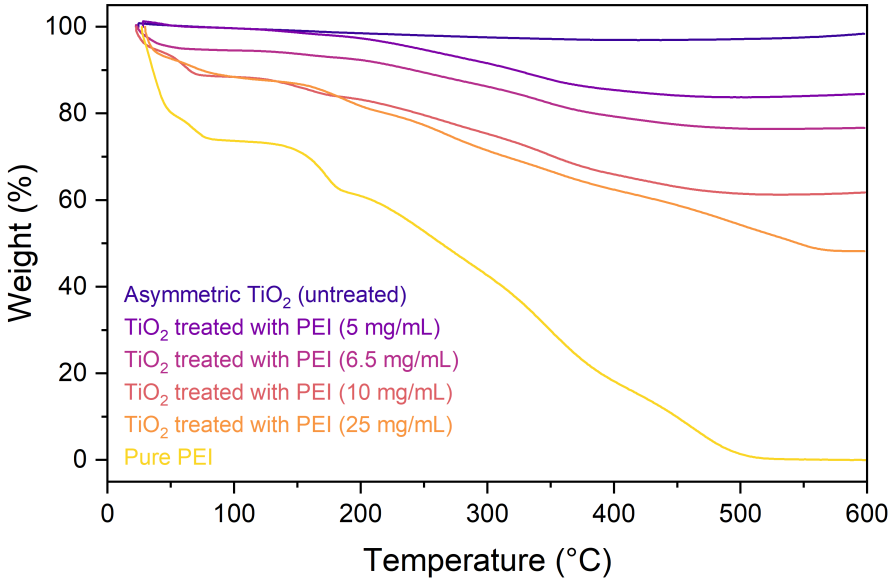

Figure A.3. TGA profiles of untreated asymmetric TiO_2, amine-impregnated asymmetric TiO_2 prepared using PEI/MeOH solutions of different concentrations, and pure PEI, as indicated.

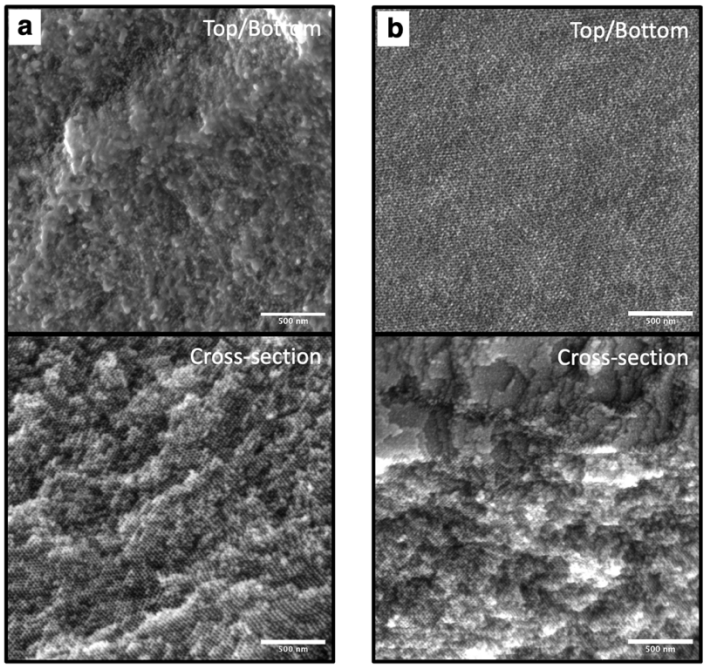

Figure A.4. SEM images of amine-impregnated TiO_2-G^A prepared using a 25 mg/mL PEI/MeOH solution: (a) without vacuum pre-treatment; (b) with vacuum pre-treatment. Surface (top) and cross-section (bottom) images are shown for each sample. As the G^A sample is homogeneous, the surface image is representative for both top and bottom surfaces.

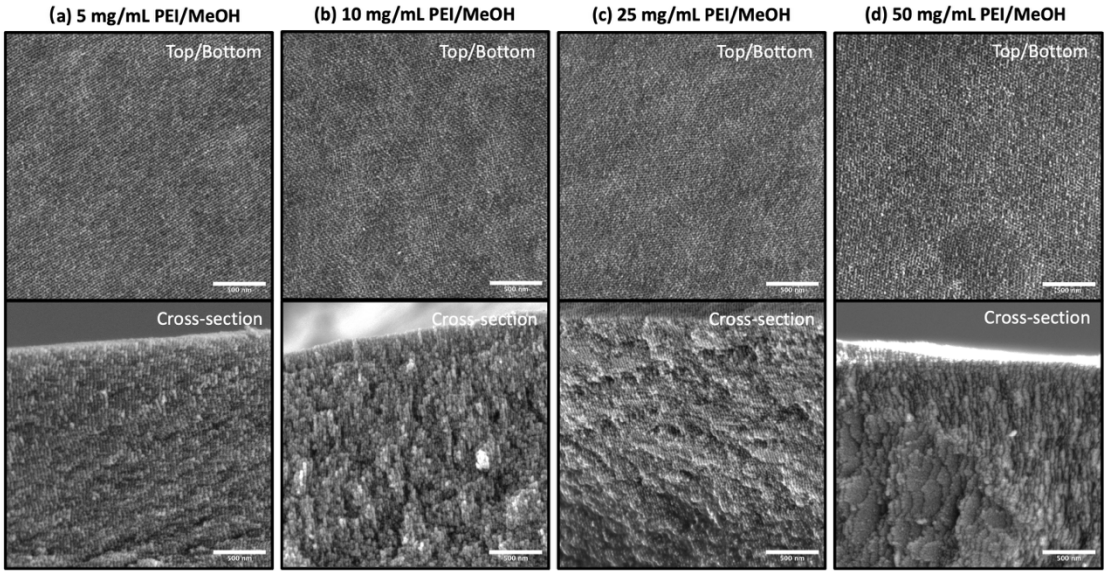

Figure A.5. SEM images of amine-impregnated TiO_2-G^A prepared using PEI/MeOH solutions of increasing concentrations: (a) 5 mg/mL, (b) 10 mg/mL, (c) 25 mg/mL, and (d) 50 mg/mL. Surface (top) and cross-section (bottom) images are shown for each sample. As the G^A sample is homogeneous, the surface image is representative for both top and bottom surfaces.

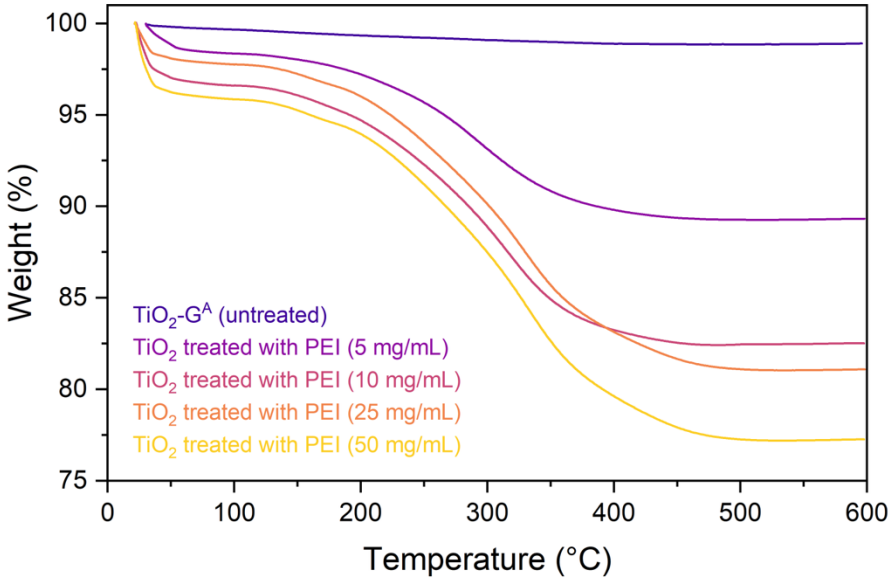

Figure A.6. TGA profiles of untreated TiO_2-G^A and amine-impregnated TiO_2-G^A prepared using PEI/MeOH solutions of different concentrations.

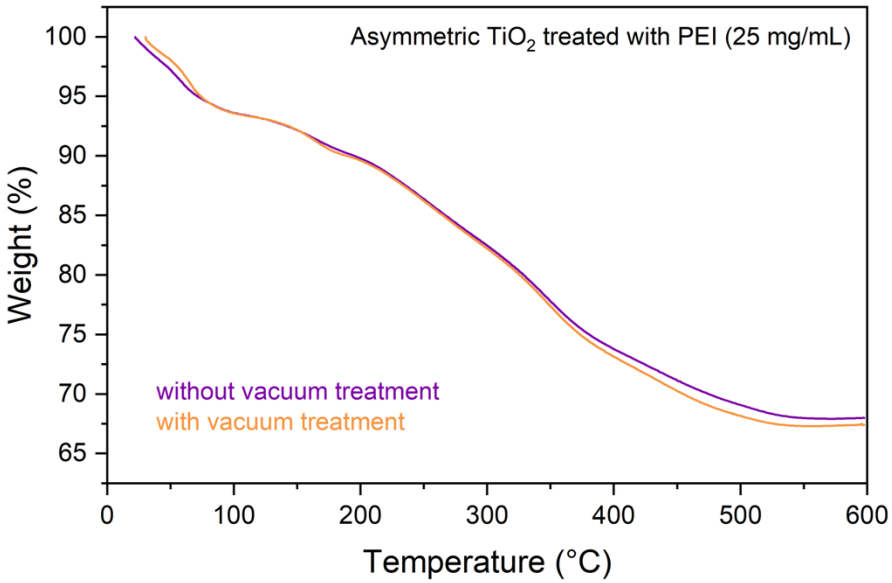

Figure A.7. TGA profiles of amine-impregnated asymmetric TiO_2 prepared using 25 mg/mL PEI/MeOH solution, with and without vacuum pre-treatment.

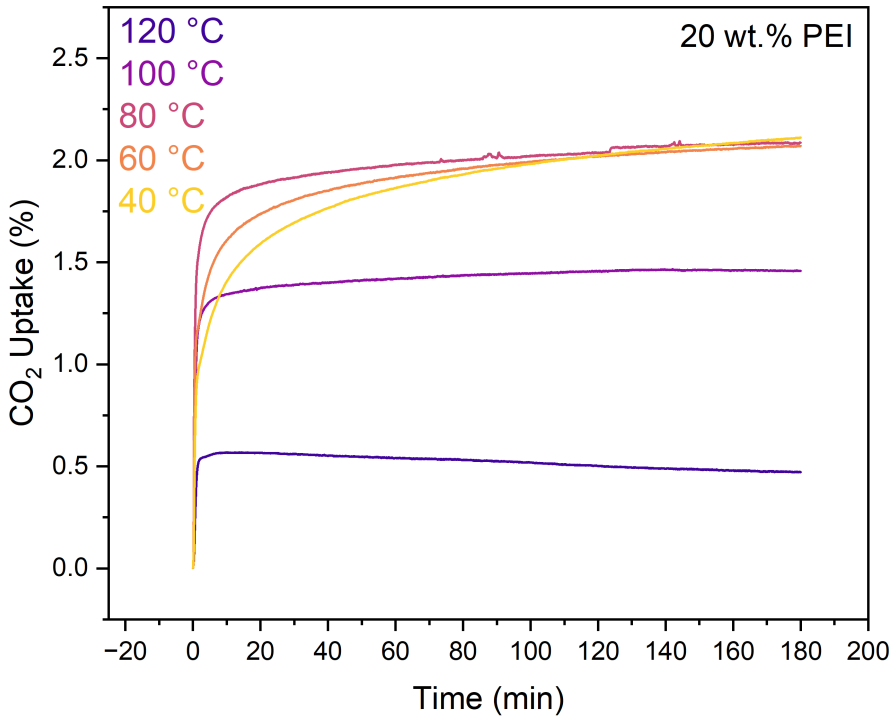

Figure A.8. CO_2 adsorption profiles of 20 wt.% PEI-impregnated asymmetric TiO_2 in 60 mL/min pure CO_2 flow at different adsorption temperatures.

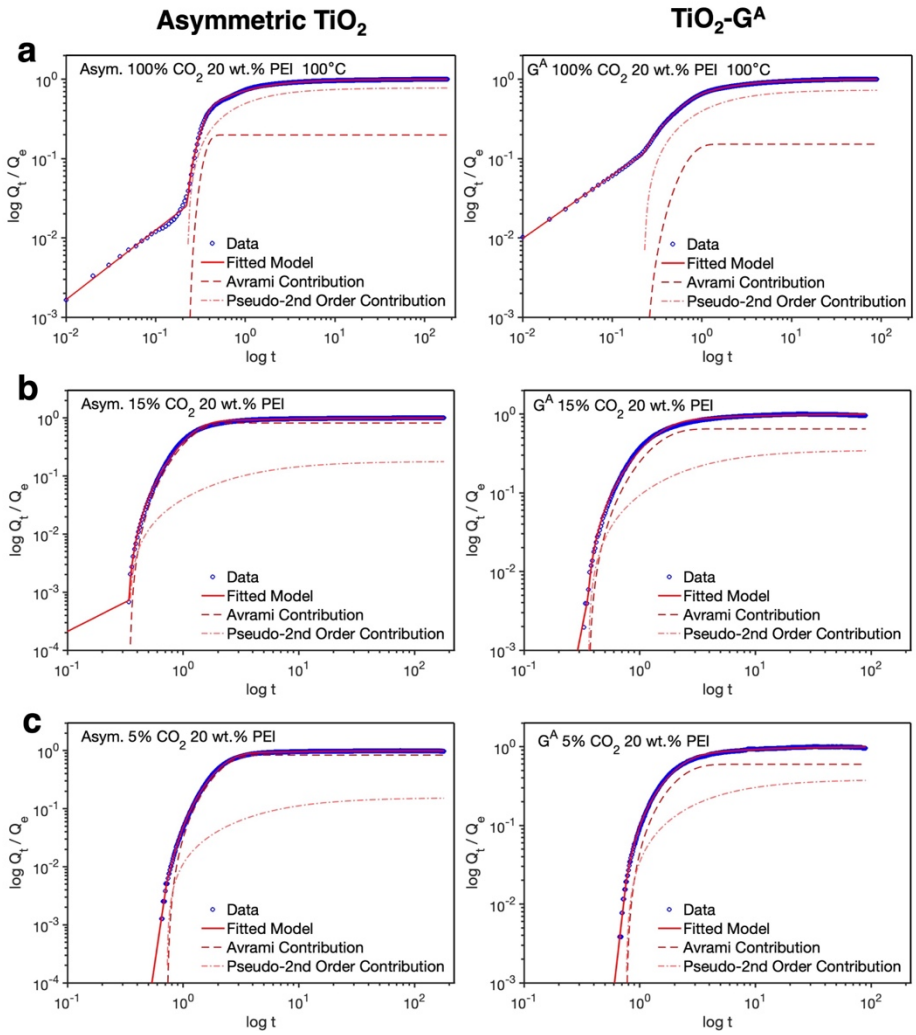

Figure A.9. Experimental results and associated log-log fittings for CO_2 adsorption at 100 °C on 20 wt.% PEI-impregnated asymmetric TiO_2 and TiO_2-G^A films at three CO_2 concentrations: (a) 100% CO_2, (b) 15% CO_2, and (c) 5% CO_2. Open symbols: experimental data; solid lines: fitted model; dashed lines: Avrami model contribution; dash-dot lines: pseudo-second order model contribution.

Table A.1. Parameters from log-log Fittings of CO_2 Adsorption at Three CO_2 Concentrations and at 100 °C on the 20 wt.% PEI-Impregnated Asymmetric TiO_2 and TiO_2-G^A samples.

CO_2 (vol %)	Sample	Stage I		Stage II			Stage III		R^2
		a_1	t_1 (min)	a_2	n	τ_2 (min)	a_3	τ_3 (min)	
100	Asymmetric TiO_2	2.56%	0.225	19.9%	2.46	0.366	77.6%	1.36	0.9989
	TiO_2-G^A	11.7%	0.224	15.2%	1.95	0.705	73.1%	1.06	0.9992
15	Asymmetric TiO_2	0.07%	0.340	82.0%	1.95	1.24	17.9%	3.90	0.9976
	TiO_2-G^A	0.53%	0.362	61.5%	1.58	1.37	37.9%	1.29	0.9965
5	Asymmetric TiO_2	0.31%	0.687	86.1%	1.92	2.23	13.6%	4.22	0.9990
	TiO_2-G^A	1.85%	0.761	59.8%	1.47	2.13	38.3%	1.45	0.9982

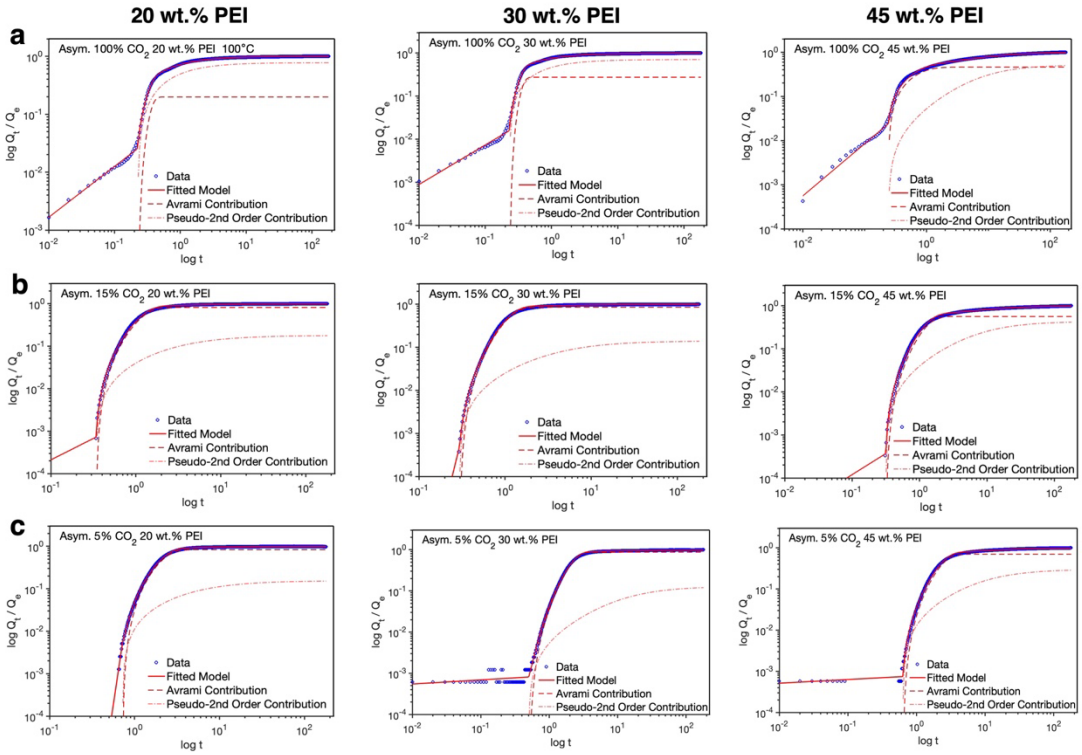

Figure A.10. Experimental results with associated log-log fittings of CO_2 adsorption at 100 °C on asymmetric TiO_2 samples with 20 wt.%, 30 wt.%, and 45 wt.% PEI loadings at three CO_2 concentrations: (a) 100% CO_2, (b) 15% CO_2, and (c) 5% CO_2. Open symbols: experimental data; solid lines: fitted models; dashed lines: Avrami model contribution; dash-dot lines: pseudo-second order model contribution.

Table A.2. Parameters from log-log Fittings of CO_2 Adsorption at Three CO_2 Concentrations and at 100 °C on Asymmetric TiO_2 Samples with 20 wt.%, 30 wt.%, and 45 wt.% PEI Loadings.

CO_2 (vol %)	PEI loading (wt.%)	Stage I		Stage II			Stage III		R^2
		a_1	t_1 (min)	a_2	n	τ_2 (min)	a_3	τ_3 (min)	
100	20	2.56%	0.225	19.9%	2.46	0.366	77.6%	1.36	0.9989
	30	1.59%	0.233	27.5%	2.75	0.371	71.0%	2.00	0.9984
	45	2.36%	0.236	46.4%	1.00	0.665	51.2%	39.7	0.9975
15	20	0.07%	0.340	82.0%	1.95	1.24	17.9%	3.90	0.9976
	30	0.04%	0.294	86.2%	2.21	1.18	13.8%	10.5	0.9983
	45	0.04%	0.318	56.6%	2.01	1.34	43.4%	25.0	0.9972
5	20	0.31%	0.687	86.1%	1.92	2.23	13.6%	4.22	0.9990
	30	0.08%	0.503	87.2%	2.45	2.32	12.7%	21.8	0.9986
	45	0.08%	0.644	68.6%	2.10	2.51	31.3%	16.9	0.9976